Ground-Based Soil Moisture Determination

François Jonard, Heye Bogena, David Caterina, Sarah Garré,
Anja Klotzsche, Alessandra Monerris, Mike Schwank, and
Christian von Hebel

Contents

F. Jonard (✉)
Institute of Bio- and Geosciences, Forschungszentrum Jülich GmbH, Jülich, Germany

Earth and Life Institute, Université catholique de Louvain, Louvain-la-Neuve, Belgium
e-mail: f.jonard@fz-juelich.de; francois.jonard@uclouvain.be

H. Bogena • D. Caterina • A. Klotzsche • C. von Hebel
Institute of Bio- and Geosciences, Forschungszentrum Jülich GmbH, Jülich, Germany
e-mail: h.bogena@fz-juelich.de; d.caterina@fz-juelich.de; a.klotzsche@fz-juelich.de; c.von.
hebel@fz-juelich.de

S. Garré
Gembloux Agro-Bio Tech, UR TERRA, Université de Liège, Gembloux, Belgium
e-mail: sarah.garre@ulg.ac.be

A. Monerris
Department of Infrastructure Engineering, University of Melbourne, Melbourne, Australia
e-mail: alessandra.monerris@unimelb.edu.au

M. Schwank
Mountain Hydrology and Torrents, Swiss Federal Institute for Forest, Snow and Landscape
Research WS, Birmensdorf, Switzerland

GAMMA Remote Sensing AG, Gümligen, Switzerland
e-mail: mike.schwank@wsl.chv

Abstract

Soil water content is a key variable for understanding and modeling ecohydrological processes. In this chapter, we review the state of the art of ground-based methods to characterize the spatiotemporal dynamic of soil water content, from point to field scale. First, point measurements methods are briefly discussed. Then, field-scale hydrogeophysical approaches such as ground-penetrating radar, ground-based L-band radiometry, electromagnetic induction, electrical resistivity tomography, cosmic-ray neutron probes, global navigation satellite system reflectometry, and nuclear magnetic resonance are described in more details. The basic principles of the different techniques, the spatial and temporal characteristics of their measurements, their advantages and limitations, as well as the recent developments in the data processing are presented.

Keywords

Soil moisture · Spatial variability · Temporal variability · Modeling · Hydrogeophysical methods

Introduction

Soil water content (SWC) is a soil physical state variable which is defined as the water contained in the unsaturated soil zone or vadose zone. Knowledge of soil water content is essential, as it represents a key variable in many hydrological, climatological, environmental, and ecohydrological processes. In hydrology, SWC plays a major role in the water cycle by partitioning rainfall into runoff and infiltration and by controlling hydrological fluxes such as groundwater recharge. Soil water content is also a key variable of the climate system, as it governs the energy fluxes between the land surface and the atmosphere through its impact on evapotranspiration (Seneviratne et al. 2006, 2010). In addition, soil water availability influences plant transpiration and photosynthesis and, therefore, has an important effect on the biogeochemical cycles (Jonard et al. 2011a).

Determining the temporal and spatial variability of SWC is hence essential for many scientific issues and applications (Famiglietti et al. 2008). In that respect, a large number of SWC sensing techniques have been developed and used in the last 50 years (e.g., Robinson et al. 2008; Vereecken et al. 2008). The standard reference method to determine SWC is the gravimetric technique, which consists of extracting soil samples from the field. The samples are then weighted before and after drying in an oven at 105 °C during 24 h to derive their water content. The amount of water in

the soil is typically expressed as volumetric [m^3 of water per m^3 of soil] or gravimetric [g of water per g of soil] water content. The gravimetric method is the only direct measurement technique, but many other techniques are available to estimate SWC. Two categories of soil moisture measurement techniques are often distinguished: contact-based (or invasive) and contact-free (or proximal/remote sensing) methods, depending on whether the methods require or not direct contact with the soil. The measurement techniques can also be classified, according to their spatial extent, as point measurement or field-scale measurement methods. Hereafter, the classification based on the spatial extent will be used.

Point Soil Water Content Measurement Methods

The most common point SWC measurement methods are the electromagnetic (EM) methods, which include time- or frequency-domain reflectometry (TDR or FDR), time- or frequency-domain transmissometry (TDT or FDT), as well as capacitance and impedance methods. The EM techniques are based on the dependency of the soil dielectric permittivity on the SWC. As the dielectric permittivity of liquid water dominates the dielectric permittivity of other soil components, water is the principal factor governing EM wave propagation in the soil.

The TDR measurement principle is based on the propagation velocity of guided EM waves emitted by a pulse generator and propagated along the waveguides of the TDR probe into the soil. The propagation velocity is determined from the measured travel time along the TDR probe (with a known length) which is dependent on the soil electromagnetic properties (Robinson et al. 2003). Similar to TDR, TDT sensors measure the propagation velocity of EM waves, but, in this case, the EM waves propagate along a closed transmission line. The measurement principle of the capacitance sensor is to incorporate soil medium that surrounds the sensor prong as part of the dielectric of the sensor capacitor. The permittivity of the soil is then determined by measuring the charge time from a starting voltage to a voltage with an applied capacitor voltage. Typically, capacitance and impedance sensors operate at a frequency between 50 and 150 MHz, while TDR/FDR and TDT/FDT sensors operate at higher frequencies. TDR/FDR and TDT/FDT sensors are then considered to be more accurate as their soil measurements are expected to be less influenced by the electrical conductivity and the imaginary dielectric permittivity of the soil.

All these instruments can perform continuous nondestructive measurements of SWC over a wide range of soils and with a very high temporal resolution. However, they are all invasive methods, which are restricted to local observation areas (< 1 m^2), and may not be representative of the soil moisture variability within the field.

Other point SWC measurement methods are also available, such as neutron probes, which are based on the estimation of the number of hydrogen nuclei in soils; heat pulse sensors, which are based on the estimation of soil thermal

properties; and fiber optic sensors, relying on the attenuation or reflection of a light signal in the soil or the characteristics of hydrophilic polymers.

Wireless Sensor Network

More recently, an emerging technology, the wireless sensor network using cluster of point SWC measurement sensors, appeared as a promising approach to monitor SWC over large areas and with a high temporal resolution, which is particularly useful for observing ecohydrological processes (Bogena et al. 2010; Jin et al. 2014b). However, given the small support scale of the sensors, i.e., the area or volume integrated by an individual measurement, and the relatively large spacing between them, these networks do not allow to reveal the local-scale SWC patterns.

Because of the multitude of SWC measurements within the sensor network, the interpretation of the sensor signal should be straightforward and unambiguous as possible. Also, the cost of the SWC sensors should be reasonably low in order to maximize the number of sensor nodes. Capacitance and FDR sensors are relatively inexpensive and easy to operate and have been found to be a promising choice for SWC measurements with wireless sensor networks. A multitude of wireless communication technologies have been used for the development of wireless sensor networks, e.g., ZigBee, Bluetooth, Wibree, and Wi-Fi (Aqeel-ur-Rehman et al. 2014). The ZigBee wireless communication technology (IEEE 802.15.4) is mostly used for wireless sensor networks due to its low-cost and low-power consumption property. Typically, three different components are present in a wireless network application: a coordinator that initiates the wireless links within the network, router devices that pass data within a network, and the sensor nodes, which can host one or more sensors.

Recent applications of wireless sensor networks include monitoring of soil moisture combined with salinity in irrigated fields to optimize irrigation management (Yu et al. 2013), spatiotemporal observation of SWC in forested sites (Rosenbaum et al. 2012), and validation of remote sensing data (Bircher et al. 2012).

Field-Scale Hydrogeophysical Methods

Hydrogeophysical methods such as ground-penetrating radar (GPR), ground-based microwave (L-band) radiometry (MR), electromagnetic induction (EMI), and electrical resistivity tomography (ERT) are increasingly used to characterize the subsurface at the field scale.

Recently, novel promising geophysical technologies such as the use of cosmic-ray neutron probes (CRNP), global navigation satellite system reflectometry (GNSS-R), and nuclear magnetic resonance (NMR) have also been investigated to characterize the SWC variability at the field scale.

Ground-Penetrating Radar

Ground-penetrating radar (GPR) is a geophysical method that uses the propagation of EM waves in the subsurface. The propagation can mathematically be described by Maxwell's equations. In common practice, GPR uses a transmitter antenna (Tx) which emits electromagnetic waves. These waves are interacting with the surrounding medium and scattering; reflections and refractions of the wave can occur (Fig. 1a). The resulted signal can be sensed via a receiving antenna (Rx). The material properties affect the velocity and the attenuation of the EM wave. The electromagnetic wave velocity (v) depends on the relative dielectric permittivity (ε_r), whereas the attenuation (α) of the wave is related to the electrical conductivity (σ) of the medium through which the wave travels. The magnetic permeability (μ) is often simplified to the value in free space ($\mu_0 \approx 4\pi \ 10^{-7}$ H m^{-1}). For high-frequency ($f > 10^5$ Hz), low-loss, and nonmagnetic materials, the permittivity and the electrical conductivity can be expressed by

$$\varepsilon_r = \left(\frac{c}{v}\right)^2 \tag{1}$$

and

$$\alpha = \frac{\sigma}{2}\sqrt{\frac{\mu}{\varepsilon}} \tag{2}$$

where c is the speed of light in free space ($\approx 3 \ 10^8$ m s^{-1}). For convenience, ε_r is often used, whereas it is described by $\varepsilon_r = \varepsilon/\varepsilon_0$ with ε the absolute dielectric permittivity of the medium (F m^{-1}) and ε_0 the free space dielectric permittivity ($\varepsilon_0 \approx 1/36\pi \ 10^{-9}$ F m^{-1}). The geophysical responses caused by changes in permittivity and/or electrical conductivity can be linked to hydrogeologically relevant variables and soil properties such as SWC, porosity, water salinity, permeability, fluid content, pore structure, clay content, soil texture, and lithological variations. Due to the large disparity of the relative dielectric permittivity of air ($\varepsilon_r = 1$), soil minerals ($\varepsilon_r = 3$–5), and pure water ($\varepsilon_r = 80$ at 20 °C), permittivity can be used to determine the water content or porosity (in the case of a saturated medium) in the vadose zone or an aquifer. For example, wet sand has a permittivity range of 20–30, whereas completely dry sand has a permittivity range of 3–5. In contrast, the attenuation of the EM wave depends strongly on the electrical conductivity of the medium, which can give indications about clay content or the pore water salinity (Davis and Annan 1989). Therefore, GPR is well in providing soil water content and furthermore well suited to monitor infiltrations and recharge processes of aquifer systems and the critical zone.

Another important aspect of GPR is the frequency of the used antenna. Most available GPR systems are using a center frequency (f_c) between 10 MHz and

3.6 GHz. The frequency corresponds to the dominant wavelength (λ_c) of the signal and can be described by

$$\lambda_c = \frac{v}{f_c}.$$ (3)

The attenuation of the wave is combination of the electrical and the scattering losses and increases with increasing frequencies (Jol 2009). Lower frequencies have a larger wavelength and can penetrate deeper (depending of the attenuation), whereas higher frequencies have a smaller wavelength and less penetration but a higher resolution.

For measuring with GPR, several different configurations can be applied: surface, crosshole, and off-ground GPR. In the last decades, all of these methods have become more and more popular and showed a high potential to derive SWC at different scales. Before we discuss these different configurations, the petrophysical relationships that can be used to derive SWC from GPR data are described.

Petrophysical Relationships for GPR and Other Electromagnetic Methods

To obtain porosity or SWC from the permittivity and electrical conductivity distribution, soil petrophysical relationships are necessary. There are numerous empirical petrophysical relationships that can be used to obtain SWC from permittivity data. One of the most common ones relating permittivity to SWC is the Topp equation (Topp et al. 1980) given by

$$\theta_v = -5.3 \ 10^{-2} + 2.92 \ 10^{-2}\varepsilon_r - 5.5 \ 10^{-4}\varepsilon_r{}^2 + 4.3 \ 10^{-6}\varepsilon_r{}^3$$ (4)

where θ_v is the volumetric water content in $m^3 \ m^{-3}$. This equation uses a third-order polynomial function fitting observed laboratory permittivity responds of sand and loam soils under different soil water contents using TDRs. There are several other relationships available based on the Topp equation (overview by Steelman and Endres 2011). Nevertheless, this model is often inaccurate for clay- and organic-rich materials. A more theoretical approach to obtain soil water content from permittivity is the dielectric mixing model. Thereby, the permittivity of the bulk material ($\widetilde{\varepsilon}$) is related to the volume fraction and the permittivity of each of the soil components in the system (e.g., Steelman and Endres 2011). The general form is given by

$$(\widetilde{\varepsilon})^\alpha = \sum_{i=1}^{n} \chi_i(\varepsilon_i)^\alpha$$ (5)

where n is the number of dielectric components in the medium, α is the geometrical fitting parameter, and χ_i is the volume fraction of the component i. Typically near-surface soils can be described by a three-phase system using air, water, and soil components under consideration of the soil porosity Φ

$$\theta_V = \frac{\widetilde{\varepsilon}^\alpha - (1 - \Phi)\varepsilon_s^\alpha - \Phi\varepsilon_a^\alpha}{\varepsilon_w^\alpha - \varepsilon_a^\alpha} \tag{6}$$

where ε_a, ε_w, and ε_s represent the relative dielectric permittivity of the air, water, and soil contributions, respectively.

This model can be extended to any number of known fractions in the soil, for example, splitting the soil component into clay and sand contributions. Fully saturated media can be described with a two-phase system using water and soil contributions. The geometrical fitting parameter α can vary between -1 and 1. By using $\alpha = 0.5$, the complex refraction index model (CRIM) is derived (Birchak et al. 1974), which showed adequate results in many studies (e.g., Roth et al. 1990):

$$\widetilde{\varepsilon} = \left[\theta_V\sqrt{\varepsilon_w} + (1 - \Phi)\sqrt{\varepsilon_s} + (\Phi - \theta_V)\sqrt{\varepsilon_a}\right]^2. \tag{7}$$

Surface GPR

For surface applications of GPR, we discriminate between two acquisition types. The common-offset (CO) reflection profiling survey, which is most widely used, has a fixed spacing between transmitter and receiver antennas at each measurement location (Fig. 1b). This technique allows fast mapping over large-scale structures. Thereby, the reflected signal is measured, indicating changes of the geophysical properties. Changes in reflection time and amplitude indicate variations in velocity
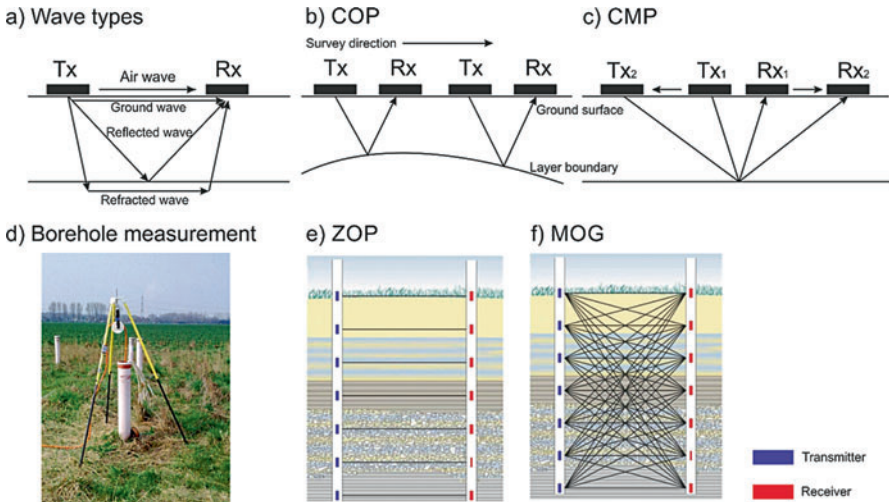
Fig. 1 Schematic GPR measuring setups for surface and crosshole measurements. (**a**) Illustrates the different wave types that can occur in a GPR survey. Surface measurement techniques are displayed in (**b**) common-offset profiling and (**c**) common-midpoint profiling. (**d**) Shows crosshole GPR measurements in the field, whereas (**e**) and (**f**) illustrate the zero-offset profiling and multi-offset gathers measuring technique, respectively

(permittivity), reflection coefficient, and attenuation (electrical conductivity). This method is normally applied at straight lines or on rectangular grids allowing a 3-D view. CO surveys provide radargrams displaying time versus distance. To convert the time into depth, the velocity of EM waves in the near surface needs to be known.

Common-midpoint (CMP) or wide-angle reflection and refraction (WARR) measurements can provide velocity information of the subsurface by varying the transmitter and receiver spacing (Fig. 1c). For CMP measurements, the transmitter and receiver antennas are moved with a fixed step size away from each other, while for WARR, the transmitter antenna is fixed at a certain point, and the receiver antenna is moved away or toward the antenna with a constant step size. Velocity semblance analysis can be applied to convert the observed reflection travel time to velocity-depth profile as well as to exploit the dielectric permittivity (Jol 2009). A definition of the structural organization of soil and soil layering can just be carried out when the contrasts in the physical properties is significant and the layer thickness is not too small compared to the wavelength of the signal. The direct ground wave that travels in the upper centimeters of the subsurface can be linked to water content using petrophysical parameters (Fig. 1c, e.g., Huisman et al. 2003). For studying soil water content over a large area, CO are suitable, whereas CMP or WARR acquisitions can provide depth information and permittivity changes at specific points with a higher resolution.

Recently, full-waveform developments are progressively done to obtain from CMP or WARR permittivity, electrical conductivity and layer depth information (Busch et al. 2012). The application of a full-waveform inversion (FWI) scheme can reliably estimate the permittivity and the conductivity for the same sensing volume, by analyzing reflected waves presented in surface WARR GPR. Busch et al. (2012) proposed a full-waveform inversion based on 3-D frequency-domain solution of Maxwell's equations assuming a layered model of the subsurface and reliably obtained permittivities, electrical conductivities, and layer depths. By obtaining two physical parameters at the same time, an improved characterization of the subsurface soil properties is possible.

Crosshole GPR

Crosshole GPR is minimal invasively and cannot be applied at large scale easily because of the need of boreholes. Nevertheless it can provide a higher resolution and insight in the medium than other techniques. For measuring bistatic cross-borehole GPR, two different measuring techniques can be applied. Zero-offset profiling (ZOP) is performed by systematically simultaneously lowering or rising the transmitter and the receiver antennas stepwise to the same depth in two different boreholes (Fig. 1d–e). Thereby, a 1-D velocity profile of the medium in between two boreholes can be achieved by assuming horizontally traveling ways and slowly changing properties. In heterogeneous soils, not only a direct wave occurs but also scattered waves caused by reflections and refractions at layer boundaries and changes in physical contrast.

An improved, but more time consuming, measuring method is multi-offset gather (MOG) shown in Fig. 1f. Thereby, the transmitter antenna is fixed at a certain

position in one borehole, while the receiver antenna is moved constantly to different locations in another borehole. This is repeated for several positions of the transmitter and guarantees that the medium between the boreholes is sampled by a large number of rays with a larger number of angles. To improve the resolution, reciprocal measurements can be collected. MOGs are commonly applied for tomographic inversion that is used to derive physical parameters in the subsurface from geophysical data. Standard ray-based inversion methods applied to crosshole GPR data use the first arrival times and the first cycle amplitude information of the measured traces. These methods use only a small amount of the measured data, and therefore their resolution is limited. In the presence of small-scale structures, for example, related to high porosity zones, these methods often cannot provide sufficient good results. To resolve such small-scale structures, a more sophisticated method is necessary. In recent years, the full-waveform inversion of crosshole GPR data has proven a high potential to resolve decimeter-scale structures that could not be detected by standard ray-based methods (Klotzsche et al. 2012). The full-waveform inversion is based on solving Maxwell's equation and uses all the information contained in the measured traces, including reflection and refraction events (Ernst et al. 2007; Meles et al. 2010). This method has been applied to several different aquifers in Germany (Güting et al. 2015), Switzerland (Klotzsche et al. 2013), and the USA (Klotzsche et al. 2014) and showed high-resolution images of small-scale structures. Comparison with porosity logging data confirmed the presence of the resolved structures.

Off-Ground GPR

Similar to surface GPR, off-ground GPR is noninvasive and can be easily and fast applied to measure field-scale SWC variations. Typically, the off-ground GPR system is based on international standard vector network analyzer (VNA) technology, thereby operating in the frequency domain, and an accurate 3-D modeling of GPR wave propagation in the antenna-soil system (Lambot et al. 2004). The VNA can be connected to an ultrawideband and highly directive horn antenna acting simultaneously as transmitter and receiver (i.e., monostatic configuration). In general, the penetration depth is less than for surface GPR. The method is also sensitive to soil surface roughness as the EM wave reflection on the soil is dependent on the surface roughness with respect to the wavelength of the EM wave. A distinction can be made between smooth and rough surfaces based on the Rayleigh criterion ($hc = \lambda/8 \cos(\gamma)$, where hc is the critical height of the surface protuberances, γ is the incidence angle, and λ is the wavelength). However, soil surface roughness can be accounted for in the inversion of off-ground GPR data for SWC retrieval by combining a roughness model to the GPR model as proposed by Jonard et al. (2012). This proximal sensing GPR method proved to be particularly appropriate for field-scaleSWC mapping and monitoring at a high spatial resolution, due its rapidity and to the air-launched configuration of the antenna (Minet et al. 2012; Jonard et al. 2013). Recently, off-ground GPR has also been successfully applied to characterize forest litter (André et al. 2016).

Summarizing, GPR is able to provide SWC and detailed information about soil properties. Thereby, different measurement techniques are possible, and new and

sophisticated inversion approaches are able to derive high-resolution images of the subsurface and allow an improved understanding of the spatiotemporal variability of SWC at different scales.

Ground-Based L-Band Radiometry

Almost 35 years ago, it was suggested that soil water content could be retrieved from remotely sensed thermal radiance received with an L-band (1–2 GHz corresponding to vacuum wavelengths of 30–15 cm) radiometer (Schmugge 1985). The radiance T_B^p (also referred to as brightness temperature) emitted from a terrestrial surface at horizontal (p = H) or vertical (p = V) polarization depends on the effective temperature T_S of the soil and on the reflectivity R^p of the observed scene via T_B^p $\approx T_S$ $(1 - R^p)$. Sensitivity of T_B^p with respect to volumetric SWC [m^3 m^{-3}] is established through R^p, being dependent on the soil effective permittivity ε_S. The latter is a strong function of SWC due to the marked contrast between the permittivity of free water ($\varepsilon_r \approx 80$ for frequencies significantly smaller than the relaxation frequency ≈ 10 GHz) and dry soil ($\varepsilon_r \approx 3$ to 5) (see also section "Ground Penetrating Radar"). The just-mentioned relationship allows the soil surface water content to be estimated from T_B^p measured with an L-band radiometer by applying dielectric mixing (e.g., Dobson et al. 1985; Mironov et al. 2009) and radiative transfer models (e.g., Mo et al. 1982; Wigneron et al. 2007). Typically, L-band brightness temperatures T_B^p of a very dry bare soil can be 150 K higher than T_B^p for the same soil in its saturated moisture state. However, in many cases, a number of more complex radiative transfer processes complicate the retrieval of SWC from remote measurements of L-band brightness temperatures. For example, parameterization of ground roughness is critical for the use of microwave radiometry (MR) to achieve quantitative information on SWC, because soil roughness heavily impacts L-band emission T_B^p and thus affects SWC retrieved from it.

However, L-band radiometry is the most adequate remote sensing technique to monitor SWC since (i) passive L-band measurements T_B^p exhibit relatively large sensitive volumes as a consequence of moderate absorption and scattering in natural media such as soil, snow, and vegetation; (ii) impacts of soil surface roughness are less distinct compared with passive measurements at higher frequencies and also active measurements (radar) even at the same frequency; (iii) measurements T_B^p can be performed at almost any time because the atmosphere is largely transparent at the L-band and the T_B^p do not depend on sunlight; and (iv) the frequency range 1,400–1,427 GHz within the microwave L-band (1–2 GHz) is protected, which means that distortions of measured T_B^p due to man-made radio-frequency interferences (RFI) are minimized.

At the plot scale, SWC can be monitored with ground-based L-band radiometers mounted, e.g., on towers (de Rosnay et al. 2006; Guglielmetti et al. 2008; Schwank et al. 2012; Jonard et al. 2015) or mobile platforms (Jonard et al. 2011b; Temimi et al. 2014). As examples, Fig. 2 shows the ETH L-band radiometer II (ELBARA II)

Fig. 2 L-band radiometer ELBARA II mounted on a tower at the MELBEX III site in Spain used for the calibration and validation of Soil Moisture and Ocean Salinity (SMOS) satellite observations

(Schwank et al. 2010) operated on a tower at the Mediterranean Ecosystem L-band Characterization Experiment III (MELBEX III) field site in Spain (Schwank et al. 2012), and Fig. 3 shows the ELBARA II operated on an arc (at $\approx$ 4 m height) in a controlled setup consisting of a sand box surrounded by a wire grid at the Terrestrial Environmental Observatories (TERENO) field test site in Selhausen, Germany (Jonard et al. 2015).

The technical specifications of the ELBARA II instrument can be considered as typical for ground-based L-band radiometers in application to the detection of SWC. As any L-band radiometer, it is a highly sensitive receiver for microwaves within the frequency band ranging from 1400 to 1427 GHz. This frequency band has become a protected radio astronomy allocation worldwide, in which it is forbidden to transmit any kind of electromagnetic radiance. An RFI-free environment is mandatory to measure brightness temperatures T_B^p emitted from terrestrial surfaces. However, the restriction of the receiver sensitivity to the bandwidth $B = 27$ MHz of the protected band implies that the received power level $P = k\ T\ B \approx 0.11\ 10^{-12}$ W (≈ -99.5 dBm) is very low (example for the observation of a black body at

Fig. 3 Controlled setup for active and passive microwave remote sensing studies at the TERENO test site in Selhausen, Germany. The setup consists of an ELBARA II radiometer mounted on an arc and a sand box in the center of a wire grid.

temperature $T = 300$ K; $k = 1.380658 \ 10^{-23}$ J K^{-1} is the Boltzmann constant). To reliably detect radiance of such extremely low power, the radiometer must be very well temperature stabilized, and its residual noise (mostly caused by transmission losses) must be kept as low as possible. Beyond that, the gain of the radiometer microwave assembly must be very high ($\approx$80 dB), linear, and as stable as possible. Furthermore, the radiometer must be equipped with at least two internal calibration sources with known reference noise temperatures. This is needed to convert the raw data at the output of the power detector into calibrated brightness temperatures T_B^p.

A further highly critical component of any L-band radiometer is the antenna attached to the microwave receiver. In most cases, it features horizontal ($p = $ H) and vertical ($p = $ V) polarization, with the highest possible insulation between the H and V ports and lowest possible return loss. To allocate measurements T_B^p with a well-defined footprint area, the antenna requires a high spatial directivity. This requirement is driven by the fundamental resolution limit defined by Abbe's law of diffraction, implying that the diameter d of the antenna aperture must be significantly larger than the observation wavelength $\lambda \approx 21$ cm. For example, to achieve a beamwidth (at -10 dB sensitivity with respect to its sensitivity along the main direction) of $\Theta \approx \pm \ 12°$ around the antenna main direction, the required diameter of the aperture is $d \approx 1.4$ m. To comply with these requirements, a suitable antenna is necessarily rather bulky as can be seen in the example shown in Fig. 2. Of course,

spatial resolution of a ground-based passive L-band observation is not only given by the antenna beamwidth Θ. The spatial extent of the footprint area at the ground results from the projection of the sensitive cone of the antenna (with aperture angle Θ) and the measurement configuration defined by the observation angle φ relative to nadir, and the radiometer installation-height H above ground. For the example shown in Fig. 2, the resulting footprint is an ellipse with long and short half-axes of $\approx$12 m $\times$ 7 m corresponding to an area of $\approx$264 m^2.

Temporal resolution of ground-based passive L-band measurements T_B^p can be rather high (order of seconds). The limiting factors with respect to the temporal resolution of SWC retrievals derived from $T_B^p(\varphi)$ are given by the requirement of multiangular measurements (e.g., $20° \leq \varphi \leq 60°$ in steps of $10°$). Hence, the time used to direct the antenna to the different elevation angles φ and the integration time (e.g., 2 s) of measurements are the limiting factors for the temporal resolution of retrieved SWC.

The use of multiangular brightness temperatures $T_B^p(\varphi)$ measured at horizontal ($p = $ H) and vertical ($p = $ V) polarization is of advantage to estimate SWC especially for vegetated areas. It allows to disentangle radiative contributions associated with SWC and vegetation properties such as optical depth τ and single-scattering albedo ω. This is because of the qualitatively different impacts of SWC and vegetation on the angular pattern of $T_B^p(\varphi)$. In most cases, dense vegetation with high microwave attenuation (corresponding to high values of optical depth τ) and possibly significant volume scattering (corresponding to high values of single-scattering albedo ω) diminishes polarization difference, while polarization difference increases with increasing SWC as the result of increasing Fresnel-like emission of the soil surface. However, beyond the advanced physically based retrieval methodologies applied to estimate SWC from $T_B^p(\varphi)$ at L-band, a number of new approaches aiming to estimate other relevant land surface parameters from $T_B^p(\varphi)$ measured at L-band are currently under development. For example, this includes the retrieval approaches applicable to the (i) detection of annual soil freeze/thaw cycles across mid to high latitudes (Rautiainen et al. 2014), (ii) estimation of snow mass-density (Lemmetyinen et al. 2016), (iii) monitoring of drought and flooding events, (iv) estimation of soil hydraulic properties (Jonard et al. 2015), and (v) estimation of vegetation water content linked with retrieved vegetation optical depth τ (Lawrence et al. 2014).

Electromagnetic Induction

Electromagnetic induction (EMI) instruments measure contactless the bulk soil electrical properties and are particularly working well in electrical conductive environments, where the SWC, soil texture, salinization, fertilization, organic matter, and/or the residual pore water contribute to the recorded apparent electrical conductivity (ECa). To estimate the SWC at the catchment scale with a high lateral and vertical resolution, EMI instruments show a particular large potential because of their mobile use that allows to measure relatively large areas in comparable short time.

The EMI method was successfully used to measure and predict the temporal and spatial SWC changes, where a linear relationship between ECa and SWC was derived using data measured simultaneously over a period of 16 months along an approximately 2-km-long transect (Sheets and Hendrickx 1995). The soil water dynamics at a 4-ha-large deltaic zone were obtained by using repeated EMI measurements over several months to discriminate the time-invariant soil properties (e.g., clay content) and the dynamic SWC changes to ECa. In addition, measurements performed before and after a heavy rainfall event identified zones of water depletion and accumulation (Robinson et al. 2009). In a subsequent EMI time-lapse study performed in asemi-arid oak savanna catchment of 4 ha size, Robinson et al. (2012) estimated the relative SWC changes by subtracting the areal ECa values of the driest day from data collected during wetter phases. Consequently, (time-lapse) EMI measurements provide important insights into the soil water distribution and dynamical changes (Calamita et al. 2015) such that EMI surveys can preferably be used over classical SWC measurements (e.g., gravimetric soil sampling and time-domain reflectometry) because these methods are laborious when covering large areas and deliver limited depth and sparse spatial point-scale information.

However, soil is inherently complex and many factors beside the soil water content determine the geoelectrical properties such that a one-to-one relation of ECa to a single soil constituent does not exist. For example, Zhu et al. (2010) investigated a 19.5-ha-large agricultural test site and found that terrain attributes, depth to bedrock, and management practices mask the effect of SWC on ECa especially during dry states compared to wetter periods and at wetter locations. Similarly, the spatiotemporal variability of SWC was found to be less significant on ECa patterns compared to the stable soil properties (soil texture) as well as compared to the electrical conductivity of the soil solution in clay-poor soils (Martini et al. 2016).

The often site-specific correlations between ECa and some soil properties open broad perspectives of EMI usages. In agricultural studies, EMI surveys were applied to precision agriculture and to better understand soil-water-plant interactions (Corwin and Lesch 2003). In soil science, EMI data were successfully used to identify soil patterns andrelatively high correlations between ECa and clay content were obtained, e.g., across the north-central USA (Sudduth et al. 2005). EMI data were further used to predict soil constituents, e.g., organic matter (Altdorff et al. 2016) as well as to infer the water holding capacity of a watershed based on soil textural prediction using ECa values (Abdu et al. 2008).

EMI instruments transmit a low-frequency ($f < 10^5$ Hz) primary magnetic field (H_P) generated by an alternating current passing the transmitter coil (Tx). Due to induction phenomena, H_P induces eddy currents in an electrical conductive subsurface, which in turn generate secondary magnetic fields (H_S), in electrical conductive media (see Fig. 4a). The ratio of the superimposed H_S over H_P, i.e., $H_\mathrm{S}/H_\mathrm{P}$, is measured at the receiver coil (Rx) and related to the ground electrical properties.

The recorded ECa, i.e., the output value of common EMI instruments, reflects a weighted average value over the coil configuration-specific sensing depth or investigated soil volume. Recently developed fixed-boom multi-coil EMI instruments as
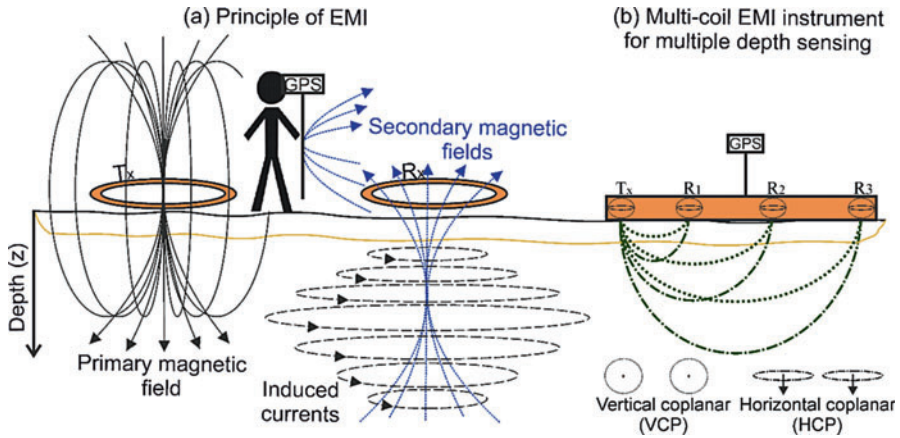
Fig. 4 (**a**) Principle of electromagnetic induction (EMI), where the transmitter Tx generates a primary magnetic field that induces eddy currents in the subsurface, which in turn generates secondary magnetic fields measured superimposed at the receiver coil Rx. Note that surrounding media may generate additional secondary magnetic fields. (**b**) Shows the principle of multi-coil EMI instruments that sense different overlapping depth intervals that depend on the coil configuration

indicated in Fig. 4b use one transmitter and multiple receiver coils that are oriented either horizontal coplanar (HCP), vertical coplanar (VCP), or perpendicular (PRP) with coil separations s ranging between 0.32 and 4 m to investigate depths of approximately 1.5 s, 0.75 s, and 0.5 s, respectively. For example, the CMD-Mini-Explorer (GF-Instruments, Brno, Czech Republic) or the DualEM-421 (DualEM, Milton, Canada) carry three and six receiver coils, respectively. The EM38 (Geonics Ltd., Ontario, Canada) houses a single Tx-Rx coil pair with $s = 1$ m to investigate up to 1.5 and 0.75 m depth in HCP and VCP mode, respectively, while also multi-frequency EMI devices, e.g., GEM-2 (Geophex Ltd., Raleigh, USA), can be used to explore different depths.

Using fixed-boom multi-coil EMI instruments, researchers attempt to obtain layered subsurface electrical conductivity models by using inverse-modeling approaches. Reliable results are obtained when inverting quantitative values. However, EMI measurements mostly record qualitative data because the induction phenomena occur in all electrical conductive media such as the operator, cables, or GPS systems surrounding the instrument, as illustrated in Fig. 4a. Quantitative EMI-ECa values were recently obtained by introducing a post-calibration procedure based on inverted electrical resistivity tomography (ERT) data (Lavoué et al. 2010). To calibrate the recorded EMI-ECa values for external influences close to the instrument, linear regressions between measured and predicted ECa values are performed, and the obtained multiplicative and additive regression factors can be applied to large-scale EMI-ECa (von Hebel et al. 2014). The approach uses collocated EMI and ERT measurements performed along relatively short calibration lines. The EMI instruments carried small (< 1.7 m) separated Tx-Rx coil pairs sensing relatively

small subsurface volumes that approximately match the ERT information. The ERT delivers the subsurface electrical conductivity distributions, which are inserted into an EMI forward model to predict ECa values along the calibration line.

The post-calibrated EMI data can be inverted quantitatively. The modeling in EMI inversions are often performed using either cumulative response functions (McNeill 1980) or a Maxwell-based exact electromagnetic forward model (EM-FM) (Wait 1951), which can be implemented due to the available computational power, to compute the response of a stratified earth to an EMI instrument. In a combined global-local search, where the global search was performed with the cumulative response functions and the local search used the exact EM-FM, post-calibrated EMI data of multiple instruments were inverted to resolve a two-layered earth along a 120-m-long transect (Mester et al. 2011). In addition, they showed that the inversion of uncalibrated data returns unreliable results. This work was adapted by von Hebel et al. (2014), who used the exact EM-FM in a parallelized three-layer inversion scheme to obtain a quasi-3-D layered electrical conductivity model of 1.1-ha-large test site. Their approach basically turned the EMI usage from a proxy indicator toward a tool that quantitatively characterizes the shallow subsurface at the catchment scale.

Large-scale EMI measurements were linked with satellite derived leaf-area index (LAI) maps (Rudolph et al. 2015) showing that the deeper subsoil is mainly responsible for plant performance especially under drought conditions. The ECa maps indicated buried paleo-river channels; however only quantitative fixed-boom multi-coil EMI data inversions reveal the depth of these channels. Here, we use the inverse-modeling scheme of von Hebel et al. (2014) to invert the post-calibrated CMD-MiniExplorer data of an approximately 3-ha-large agricultural field showing prominent paleo-river channel structures. One structure runs approximately north-south (N-S) through the middle of the field; the second prominent structure is a westward running channel that seems to be connected to the N-S structure in the northern part of the field. Two depth slices through the large-scale quasi-3-D EMI inversion results are shown in Fig. 5.

In Fig. 5a, the depth slice at 0.1 m cuts the plowing layer, where a relatively homogeneous soil and no paleo-river channels were present. The deeper slice at 1.5 m depth presented in Fig. 5b shows the prominent paleo-river channels with larger electrical conductivities due to clay-rich material compared to the low electrical conductive gravelly surrounding. In drought conditions, the paleo-river channels still supply water due to higher water holding capacity of the finer-textured soil compared to the generally sand- and gravel-dominated sediments. The inversion results additionally provided new insight into the soil-plant interaction. Whereas linear regression between LAI and ECa of VCP coils with s = 0.32 m obtained a coefficient of determination (R^2) of 0.63, the R^2 of LAI and the inverted electrical conductivity (σ) of the upper layer was $R^2 = 0.15$. These results indicate, from the EMI perspective, that the signal is more influenced by material of deeper depths than estimated by the cumulative response definition (that states that 70% of the signal originate in the coil specific sensing depth (McNeill 1980)), i.e., 0.25 m or approximately the plowing depth for the VCP coils with s = 0.32 m. For ecohydrological

Fig. 5 Quasi-3-D inverted EMI data, where x and y given in UTM coordinates, zone 32 U, and z is the depth. (**a**) Depth slice through upper 0.1 m roughly showed homogenous soil. (**b**) Slice at 1.5 m depth, where buried paleo-river channel structures with larger electrical conductivity values compared to the surrounding material were visible. Whereas the soil is generally sand and gravel dominated, the paleo-river channels are characterized by finer-textured, clay-rich, soil having inherently a higher water holding capacity to supply plants especially under drought conditions
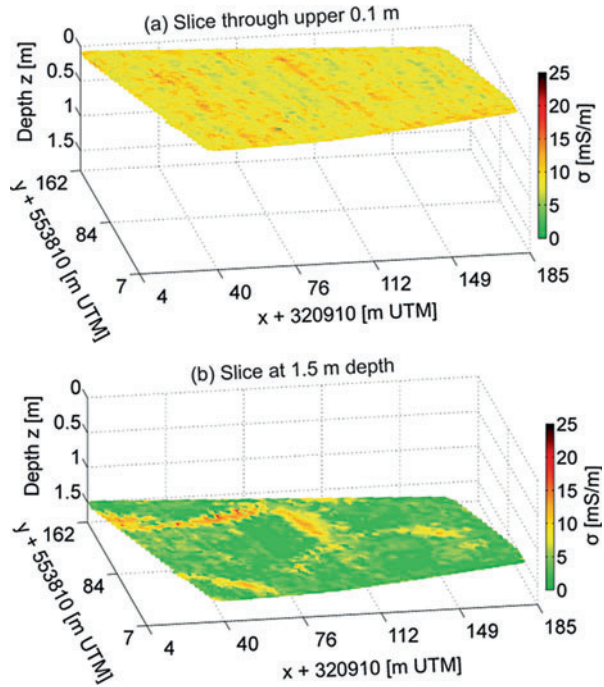
modeling purposes, inverted electrical conductivities should be used instead of ECa to accurately characterize subsurface processes.

Electrical Resistivity Tomography

Whereas electrical resistivity tomography (ERT) was initially especially used for exploration and at larger scales (geology, groundwater), it has become increasingly popular for vadose zone research in the last decades (e.g., Samouelian et al. 2005) since the commercial equipment has become more powerful and adapted to monitoring, the potential of inversion codes has improved, and computing power has increased. Electrical monitoring has been used to monitor water fluxes and solute transport under agricultural crops (e.g., Banton et al. 1997; Michot et al. 2003), show interaction for water between different species (e.g., Garré et al. 2013), or measure water depletion by trees (Cassiani et al. 2015). In addition to soil monitoring, it has been used to measure water fluxes in tree stems (al Hagrey 2006). Nevertheless, some difficulties still need to be resolved when ERT is applied at decimeter resolution in the soil-plant continuum: (i) lack of complementary measurement methods and physically based models to take into account spatially variable bio-pedo-physical relationships, (ii) difficulties to resolve sharp contrasts due to smoothness-constraint inversion (see below), (iii) lack of standardized methods to take into account measurement and model errors and their temporal variation for monitoring

studies, and (iv) practical difficulties with electrode contact arising when measuring under very dry conditions.

Electrical resistivity tomography is a technique which measures the bulk electrical resistivity of the soil between electrodes. The bulk electrical resistivity corresponds to the combined resistivity of soil particles, pore water, and air. A basic measuring system consists of four electrodes (A, B, M, N), a transmitter, and a receiver. The transmitter applies a quasi-DC current (I) (i.e., rectangular pulses or an AC current at low frequency to avoid polarization) to the ground using the electrodes A and B, whereas the receiver measures the voltage (V) between the electrodes M and N (see Fig. 6).

Figure 7 shows some possible four-electrode arrays. Resistivity meters then give a resistance (R) value for each combination of four electrodes, based on Ohm's law $R = V/I$.
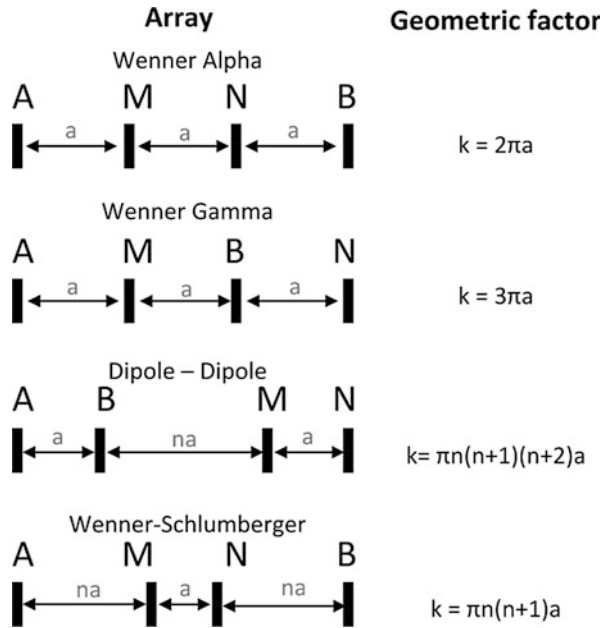
For a tomography, more than four electrodes are used. During the measurements, many different combinations of current and potential electrodes are used for injection and measurement. The electrodes can be inserted in the soil surface or at several depths as borehole electrodes or a combination of both.

From the current, the voltage and a geometric configuration factor (k), the apparent electrical resistivity (ρ_a) is calculated. The geometric factor depends on the spatial arrangement of the four electrodes A, B, M, and N. Resistance is an extrinsic property (i.e., depends on the way it is measured); resistivity is an intrinsic property (i.e., depends only on the material in which the measurement is performed). We call the obtained resistivity "apparent," because it represents the resistivity of a
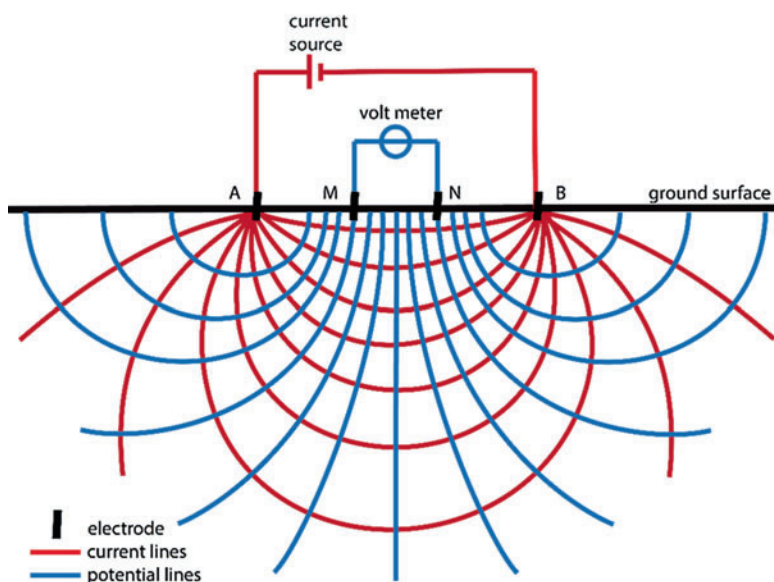
Fig. 6 Basic concept of electrical resistivity measurement of the subsurface

Fig. 7 Four exemplary standard electrical resistivity electrode arrays with corresponding geometric factor

Array   Geometric factor

Wenner Alpha — $k = 2\pi a$

Wenner Gamma — $k = 3\pi a$

Dipole – Dipole — $k = \pi n(n+1)(n+2)a$

Wenner-Schlumberger — $k = \pi n(n+1)a$

hypothetical, homogeneous medium, which will give the same resistance value for the same electrode arrangement. The measured, apparent resistivity is a weighted average of the resistivities of the various materials that the current encounters. The closer the electrode spacing, the more of the current will remain close to the surface, and the more the apparent resistivity value will be influenced by the properties and state of the material close to the surface.

The vector form of Ohm's law is the basis for resistivity studies:

$$\mathbf{J} = \sigma\mathbf{E} = \frac{1}{\rho}\mathbf{E} = -\frac{1}{\rho}\nabla V. \qquad (8)$$

where $\mathbf{J}$ is the current density vector [A m^{-2}], $\mathbf{E}$ is the electric field vector [V m^{-1}], V is the electric potential (V), σ is the conductivity [Ω m^{-1}], and ρ is the resistivity [Ω m]. The electrodes depicted in Fig. 6 are treated as point sources/sinks of current flow. For surface electrodes, the total current (I) flows across the surface of a half sphere with area $\frac{1}{2}(4\pi r^2)$, with r the radius of the sphere, and thus Ohm's law for one electrode becomes

$$J = \frac{I}{\frac{1}{2}\left(4\pi r^2\right)} = -\frac{1}{\rho}\frac{dV}{dr}. \qquad (9)$$

Integrating this for constant resistivity yields the following equation for the potential at a distance r from the electrode:

$$V(r) = \frac{\rho I}{2\pi r}. \tag{10}$$

In real field measurements, the resistivity is generally not constant, so this expression actually corresponds to the earlier defined "apparent resistivity." If we now use this to express the potential at measurement electrodes M and N, we have to superpose the potential of the two source electrodes A and B:

$$V_{\mathrm{M}} = \frac{\rho I}{2\pi} \left(\frac{1}{AM} - \frac{1}{MB} \right). \tag{11}$$

where AM and MB represent the distances between the electrodes. The total potential difference between the electrodes M and N is therefore

$$V_{\mathrm{MN}} = V_{\mathrm{M}} - V_{\mathrm{N}} = \frac{\rho I}{2\pi} \left(\left(\frac{1}{AM} - \frac{1}{MB} \right) - \left(\frac{1}{AN} - \frac{1}{NB} \right) \right) = \rho I \frac{1}{k} \tag{12}$$

with k the abovementioned geometric configuration factor, which will yield a specific value for a given electrode spacing (see Fig. 7). Note that this is true for a flat surface. If an undulated topography is present, the configuration factor is unknown and can only be assessed by numerical modeling using homogeneous resistivity (Günther 2004).

Relation to State Variables

As stated before, the bulk electrical resistivity (and its reciprocal electrical conductivity EC) or "effective electrical resistivity" is the resistivity of the solid-water-air system, which is the (un)saturated soil in ecohydrological studies. The apparent electrical resistivity (ρ_{a}) in soil depends on the water content, pore water electrical conductivity, soil porosity, surface conductivity of the solid particles as well as the soil temperature. Hence, to derive soil water content from electrical resistivity measurements, one must rely on a "pedo-electrical" function. Several of these models have been elaborated with more or less complex approaches. Without aiming at being exhaustive, we list some of these models here. A well-known EC model is the empirical Waxman and Smits (1968) model based on Archie's law (Archie 1942). In 1998 Revil and Glover proposed a more physically based model also based on Archie's law. Derived more in the context of agricultural soils, the conceptual Rhoades et al. (1989) model relies on the assumption of two separate parallel electrical pathways: a continuous pathway through large water-filled pores and a series of coupled solid-liquid pathways.

The effect of temperature on ρ_{a} is often treated before applying a pedophysical relationship to normalize the data to a reference temperature. There are two distinct effects of temperature on soil bulk electrical conductivity: (i) the mobility of the ions in the soil solution and (ii) the quantity of total dissolved solids (TDS) in the pore water, which is an irreversible process. Most of the current models for temperature correction of electrical resistivity correct only for this first factor. Ma et al. (2011)

gives an overview of temperature correction models. A temperature correction model (to convert to a reference temperature T of 25 °C) which is often used in hydrogeophysical investigation is the equation developed by Campbell (1949): $\sigma_{a\text{-}25} = \sigma_{a\text{-}T}/(1 + \alpha (T-25))$, with $\alpha = 0.02$ and σ_a the apparent electrical conductivity.

Nevertheless, the available theoretical models often fail when used without site-specific field calibration at field scale, and therefore, several researchers still prefer empirical, site-specific approaches to quantify the pedophysical relationship for their application. In those cases, SWC, electrical resistivity, and temperature are measured simultaneously in the field over a wide range of conditions and in the different soil horizons and used to establish a simple, empirical relationship (e.g., Michot et al. 2003; Garré et al. 2011).

Data Processing

The apparent resistivities of a 2-D survey are commonly visualized in the form of a pseudosection. In this diagram, the horizontal location of the point is placed at the midpoint of the set of electrodes used to make that measurement. The vertical location of the plotting point is placed at a distance, which is proportional to the separation between the electrodes. Following Edwards (1977), the vertical position is placed at the median estimated investigation depth, or pseudodepth, of the quadrupole used. This pseudodepth value is based on the sensitivity values or Frechet derivative for a homogeneous half space. The color of the point represents the apparent resistivity. A pseudosection gives a good idea of the true subsurface resistivity distribution, but not of its exact spatial organization since the contours depend on the type of array used and the true resistivity of the subsurface.

To determine the true resistivity of the subsurface, a mathematical procedure, called "inversion," must be carried out. The inversion procedure combines a forward modeling routine able to simulate the electrical field in any spatial model of resistivity distributions with a mathematical procedure to compare measured apparent resistivity values with simulated apparent resistivity values and move toward a model which suits the data well. In ERT studies, for the same measured data set, there is wide range of models resulting in the same calculated apparent resistivity values. To narrow down the range of possible models, some assumptions are made concerning the nature of the subsurface that can be incorporated into inversion subroutine. One common assumption is that smooth changes are more probable than sudden changes, a principle that is applied in the conventional smoothness-constrained inversion (de Groot-Hedlin and Constable 1990). Some commonly used inversion codes are RES2DINV/RES3DINV (Loke and Barker 1996), R2/R3T (Binley 2013), BERT (Günther 2004), and CRTOMO (Kemna 2000).

Spatial Extent, Resolution, and Sensitivity

In order to speak of the spatial extent and precision of ERT measurements, we first need to define a few concepts: depth of investigation, resolution, sensitivity, and data coverage.

Oldenburg and Li (1999) defined the depth of investigation (*DOI*) as the depth below which data no longer constrain earth structures. In their method, they require

two successive inversions with different reference models to visualize regions of parameters only related to the choice of the reference model. The index tells you how much the model is constrained by the data and how much by the regularization, and Marescot et al. (2003) and Robert et al. (2011) followed similar approaches. Since its value depends on the way it is computed, it should be considered as a qualitative index indicating whether an anomaly is more likely to be data-related or constraint-related. The *DOI* should not be confused with the pseudodepth, which is described above.

Sensitivity is related to data coverage. The sensitivity matrix (S) shows how the data set is actually influenced by the respective resistivity of the model cells, i.e., how areas of the imaging region are "covered" by the data (Kemna 2000). The Jacobian or sensitivity matrix contains the partial derivatives of the model responses with respect to the model parameters. A poorly covered region is likely to be less well resolved, but it must be emphasized that good coverage does not necessarily imply high resolution. Sensitivity and resolution are correlated but do not give the same information.

Resolution is like the filter through which the inversion process sees the subsurface, so that the inverted model equals the resolution matrix (R) times the true resistivity distribution. Ideally R is defined by an identity matrix so that the inverted model equals the true distribution. However, this is never possible for a continuous inverse problem with incomplete data (Friedel 2003). A complete description of how R is computed can be found in Günther (2004).

These different quantities can either be obtained a priori using model simulations of the object under investigations yielding probable resistivity distributions on which different possible electrode arrays can be tested for their expected performance (e.g., Garré et al. 2012). As such, an informed choice can be made in the trade-off between measurement time, resolution, and measurement volume. A posteriori, these measures can be used to assess the reliability of the inverted parameters, as pointed out by Caterina et al. (2013).

Perspectives

Recently, several authors have pointed out the potential but also the complexity of using electrical measurements to characterize the root zone moisture and/or salinity dynamics. Some authors claim to be able to use electrical measurements to localize the root system. Many different types of pedophysical relationships have been used to isolate one of these variables. However, in addition to inherent soil heterogeneity, the presence of plant roots makes the soil a highly heterogeneous medium in space (root architecture) and time (root growth, maturation, and decay) in which the distribution of the electrical field and the bio-pedo-physical properties of the medium are uncertain. On the one hand, researchers are digging into the potential of using the distinct electrical signature of root tissue in order to map their presence noninvasively. Historically, botanists have explored electrical capacitance measurements. Recently, the potential of induced polarization to map roots is being explored. On the other hand, the spatial heterogeneity of the bio-pedo-physical relationship needs to be taken into account. Typically, soil moisture or salinity values are obtained

applying one single pedophysical relationship for a given soil horizon, whereas it is clear that this relationship is heterogeneous even within one and the same horizon. The use of (geo)statistical techniques taking into account spatial (co-)variance might be a possibility. Nevertheless, it is not straightforward to obtain training images to characterize the spatial structure of this relationship.

The classical inversion approach suffers from spatially and temporally varying resolution and sometimes yields unrealistic solutions without uncertainty quantification, making their utilization for hydrogeological calibration less consistent. The inverse problem for electrical resistivity tomography is ill posed, and its solution is therefore nonunique. A regularization is used to reduce the amount of mathematical solutions to more "plausible" models. The most common regularization is the smoothness constraint, which selects a "smooth" distribution of resistivities above one with a lot of contrasts. However, the inversion can also be regularized using prior information on the system under consideration in the inversion. Recently, the addition of structural constraints in Occam's inversion (smoothness-constrained inversion) or the incorporation of geostatistical constraints has been implemented successfully. Another option is to avoid the geophysical inversion and use process models, e.g., a hydrodynamic physically based model representing the processes governing the system under consideration, to invert directly for soil hydraulic or root architectural parameters. This option is called a coupled inversion (e.g., Hinnell et al. 2010). However, the technique is difficult to apply in complex field cases and it remains computationally demanding to estimate uncertainty. Prediction-focused approaches (Hermans et al. 2016) might offer new perspectives circumventing the necessity to invert the data by seeking a direct relationship between the data and the subsurface variables we want to predict.

Cosmic-Ray Neutron Probes

Theoretical Background

Estimating and monitoring soil moisture at the appropriate spatial and temporal scale has proven to be a difficult task (Bogena et al. 2015a). One promising geophysical technique to help fill this need is the cosmic-ray neutron probe (CRNP) (Desilets et al. 2010; Zreda et al. 2008), which measures the ambient amount of low-energy secondary neutrons in the lower atmosphere. A detailed description of the CRNP technique can be found in Zreda et al. (2012). Here, only the basic principles are presented. A cascade of secondary neutrons with varying energy levels are created in the earth's atmosphere when incoming high-energy primary particles produced within supernovae interact with atmospheric nuclei (Zreda et al. 2012; Köhli et al. 2015). The secondary high-energy neutrons continue to lose energy during numerous collisions with nuclei in the atmosphere. Due to its higher density, soil effectively slows neutrons further down. In the final near-surface neutron energy spectrum, three different types of neutron energies are prominent (Köhli et al. 2015): highly energetic neutrons around 100 MeV, evaporation neutrons around 1 MeV, and low-energy neutrons which are in thermal equilibrium with the

environment (< 0.5 eV). Epithermal fast neutrons (in the following referred as "fast neutrons") with energies between 0.5 eV and 100 eV are particularly sensitive to energy loss by elastic collisions with light atoms like hydrogen. Since soil moisture is one of the largest sources of hydrogen present in terrestrial systems, it largely controls the presence of fast neutrons in the lower atmosphere (Zreda et al. 2012). Thus, relative changes in the intensity of fast neutrons are strongly correlated to soil moisture changes.

Design and Calibration of CRNP

The fast neutron intensity in the lower atmosphere can be measured by CRNP's, which are neutron detectors with a tube filled with helium-3 or boron-10 (enriched to 96%) trifluoride ($^{10}BF_3$) proportional gases at high pressure (Zreda et al. 2012). A polyethylene shielding around the tube moderates fast neutrons to thermal neutrons before they enter the detector tube, in order to increase the probability of them being captured by the detector. Within the detector tube, fast neutrons that collide with helium-3 or boron-10 nuclei produce electrons that induce pulses of electrical current and which are counted by the detector. The size of the tube determines the probability of collisions and thus the sensitivity of the CRNP to measure soil moisture at higher temporal resolution (Bogena et al. 2013). The energies measured by the bare tube comprise a continuous distribution which is heavily weighted toward thermal neutrons (< 0.5 eV), with a small proportion of fast neutrons also being detected ($< 10\%$) (Andreasen et al. 2016). The moderated detector is more sensitive to higher neutron energies (> 0.5 eV). Although the polyethylene shielding effectively attenuates the influx of thermal neutrons, a large proportion of the counts (approximately 40% of the thermal neutrons detected by the bare detector) still originates from below 0.5 eV (Andreasen et al. 2016). Since neutron counts follow Poissonian statistics, the measurement uncertainty of a given neutron intensity (N) decreases with increasing neutron intensity according to $N^{0.5}$.

Desilets et al. (2010) proposed a simple calibration function to relate fast neutron intensity measurements to volumetric soil moisture:

$$\theta_v = \rho_{bd} \left(a_0 \left(\frac{N_{corr}}{N_0} - a_1 \right)^{-1} - a_2 \right) \tag{13}$$

where θ_v is the volumetric soil water content [m^3 m^{-3}]. N_{corr} refers to the measured fast neutron counts corrected for influences of atmospheric pressure and humidity and variations in incoming cosmic radiation (see Zreda et al. 2012 for a detailed discussion). The parameters a_0 and a_2 are divided by the dry soil bulk density ρ_{bd} [g cm^{-3}]. Using simulations of neutron transport for generic silica soils, Desilets et al. (2010) derived $a_0 = 0.0808$, $a_1 = 0.372$, and $a_2 = 0.115$ for values of $\theta > 0.02$ g g^{-1}. Thus, only N_0, representing the count rate over dry soil conditions, needs to be calibrated.

This calibration function is not universal, because it depends on local soil and vegetation characteristics reflecting the variation of background hydrogen levels

across landscapes (Zreda et al. 2012). To account for these influences, it needs to be fitted using soil samples taken within the footprint of the CRNP, which typically has a radius between 150 m and 250 m and depths between 0.1 m and 0.7 m (Köhli et al. 2015). Given this large footprint area, the CRNP method is an ideal complement to long-term surface energy balance monitoring with the eddy covariance technique (Jana et al. 2016). Recent neutron transport modeling has further refined the footprint area to be a function of atmospheric water vapor, sensor elevation, surface heterogeneity, vegetation, and soil water content (Köhli et al. 2015).

The application of the CRNP method is hampered by its susceptibility to additional sources of hydrogen (e.g., above- and belowground biomass, humidity of the lower atmosphere, lattice water of the soil minerals, organic matter and water in the litter layer, intercepted water in the canopy, and soil organic matter), e.g., Bogena et al. (2013), and Heidbüchel et al. (2016). In case that these hydrogen sources are temporally stable, the influence can be amended by estimating the contribution of each source and subtracting its contribution during the transformation of the neutron counts into SWC (Zreda et al. 2012). In the following chapter, methods for correcting for biomass effects on CRNP measurements are discussed in more detail.

### Accounting for Biomass Effects on CRNP Measurements

Recently, Baatz et al. (2015) developed a simple empirical approach to correct for biomass effects based on long-term fast neutron intensity measurements from a network of 10 CRNPs located in the Rur catchment, Germany. In addition, they gathered fast neutron intensity measurements for shorter periods (between 24 and 405 h) at 13 locations in the forested research catchment Wuestebach (Germany), which was partly deforested. These locations were selected in such a way that the CRNP footprint contained distinctly different amounts of aboveground biomass. Using this extensive data set, they found that fast neutron intensity was reduced by 0.9% per kg dry aboveground biomass per m^2. Baatz et al. (2015) further developed an equation for correcting N_0 for biomass effects:

$$N_{0,\text{corr}} = -r\, ABG_{\text{dry}} + N_{0,\ ABG=0} \tag{14}$$

where $N_{0,\text{corr}}$ is the biomass corrected N_0, $N_{0,AGB=0}$ is the reference N_0 for a site without standing biomass, ABG_{dry} is the dry aboveground biomass [kg/m^2], and r represents the reduction factor for N_0. It was found that r has a value of 11.19 per kg dry aboveground biomass per m^2. This regression explained 87% of the variation between biomass and neutron count rate. It has to be noted that this correction was derived for temporally stable biomass situations (e.g., forest sites). In addition, forests typically have a litter layer, whose water content can change rapidly adding additional temporal variability to the CRNP signal. Therefore, Bogena et al. (2013) recommended considering the water dynamics in the litter layer explicitly in the calibration of the CRNP. Furthermore, temporally changing above- and belowground biomass of growing vegetation (e.g., crops) and intercepted water in the

canopy affect fast neutron count rates and calibration parameters in a complicated way. Baroni and Oswald (2015) proposed that the influence of aboveground biomass could be straightforwardly incorporated into a weighting approach. On the other hand, Coopersmith et al. (2014) found that soil moisture is overestimated for high-biomass situations, but it is underestimated when biomass is relatively low. In order to elucidate the biomass effect of growing vegetation on CRNP measurements in more detail, the field test site in Selhausen (Germany) of the TERENO project (Bogena et al. 2012) was instrumented with 7 CRNPs and a wireless soil moisture sensor network (Fuchs 2016). In order to track the biomass changes of the growing winter wheat, roots and plants were sampled approximately every 4 weeks. As expected, an increasing discrepancy between cosmic-ray-derived and in situ measured SWC during the growing season and a sharp decrease in discrepancy after the harvest were found (Fig. 8).

Figure 8 shows a good agreement between SWC derived from in situ measurements and cosmic-ray neutron data for the time period with low-standing biomass (<2 kg m^{-2}). As winter wheat begins to grow faster, SWC derived from the CRNP starts to deviate from the in situ measurements. In order to correct for the temporally varying effect of biomass on fast neutron intensity, Fuchs (2016) derived relationships between the calibration parameter N_0 and total fresh biomass. Using these relationships for the correction of fast neutron intensity reduced the discrepancy between cosmic-ray-derived and in situ measured SWC considerably (from 0.39 m^3 m^{-3} to 0.08 m^3 m^{-3}). The remaining uncertainty is due to the short-term fluctuations in the CRNP data that coincide with rainfall events, indicating effects of interception storage and sharp soil water gradients due to infiltration of rainfall water into the soil. A major further step in this direction would be the development of a method that enables the inference of biomass changes from cosmic-ray neutron
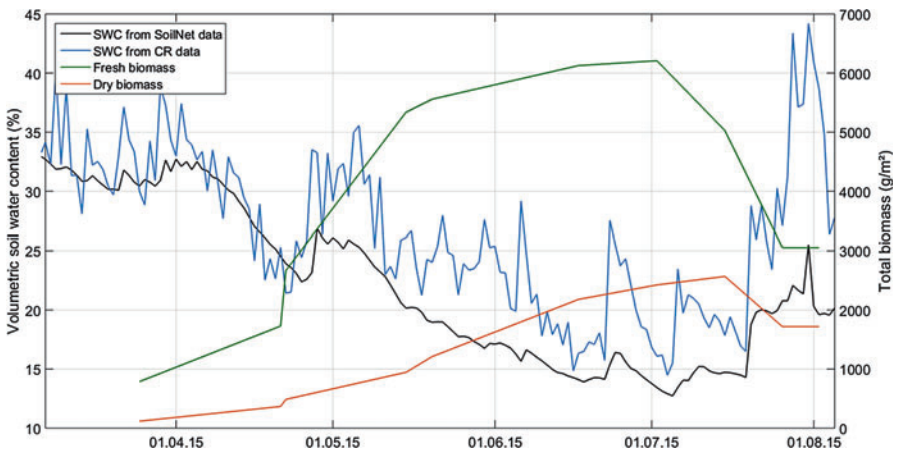
Fig. 8 Time series of soil water content derived from in situ measurements (SoilNet data) and cosmic-ray neutron data (CR), as well as measurements of fresh and dry biomass between March and September 2015 at the TERENO test site in Selhausen, Germany

intensity measurements without further measurements. Recently, it was shown that the temporal dynamics of the thermal-to-fast neutron ratio might be a potential predictor for canopy interception and biomass changes (Andreasen et al. 2016). However, to this date, no generic method exists that enables the direct dry biomass estimation without additional information on other sources of hydrogen in the footprint of the CRNP (e.g., water content of vegetation and soil).

Increasing the Spatial Scale with the COSMOS Rover

Although the CRNP footprint is already large (>10 ha), a single probe cannot capture soil moisture patterns at the catchment scale. Recently, a roving version of the CRNP (the COSMOS rover) has been developed to measure soil water content at larger scales (e.g., Chrisman and Zreda 2013). The main difference to the standard CRNP is the much larger size of the detector tubes used for the COSMOS rover, enabling measurements with much higher temporal resolutions (e.g., 1 min). The COSMOS rover thus enables the assessment of catchment-scale wetness conditions (up to hundreds of square kilometers in a single day under ideal situations). This makes the COSMOS rover a very promising method to close the critical scale gap in SWC monitoring toward the scale of a catchment. First feasibility experiments have been conducted with the COSMOS rover. For instance, Chrisman and Zreda (2013) attempted to compare road-effected rover data with SMOS satellite products. Later, Dong et al. (2014) measured and validated spatial SWC surveys with independent in situ SWC measurements. They concluded that the COSMOS rover is able to determine SWC with an accuracy of about 0.03 m^3 m^{-3}. Recently, Franz et al. (2015) combined SWC measurements from roving and fixed cosmic-ray neutron probes with the aim to establish a real-time monitoring system for irrigation management. One of the major challenges is the calibration of the sensor under mobile conditions, since spatial variations in vegetation biomass and soil properties strongly affect the neutron counts. Therefore, in order to achieve a reliable estimation of spatial SWC, a new concept for signal processing is required that incorporates information of biomass distributions and soil properties in the calibration process.

Global Navigation Satellite System Reflectometry

The concept of Global Navigation Satellite System Reflectometry (GNSS-R) was first introduced 20 years ago, although it was years later when its use for remote sensing of environmental variables was finally considered. GNSS-R has several advantages over other technologies: all-weather and worldwide availability of GNSS signals; it is inexpensive and consists of lightweight, low-power consumption sensors; there are an increasing number of GNSS satellites in orbit; and GNSS operate in L-band (with wavelengths ≈ 20 cm) which is one of the optimal frequency bands for surface soil moisture estimation. Altogether, this highlights the potential of GNSS-R for near real-time monitoring of land properties, such as surface SWC, vegetation water content (VWC), and snow depth. Over land, GNSS-R takes advantage of the multiple GNSS satellites visible at any time and at various elevation

angles, and also of the high sensitivity of the reflected signal to changes in the dielectric constant (and therefore SWC) of the ground. Although the development of a robust SWC retrieval algorithm from GNSS-R observations is a work in progress, a few algorithms have been derived for bare and vegetated surfaces using electromagnetic forward models and widely used dielectric constant models (Jin et al. 2014a; Zavorotny et al. 2014; Larson 2016). Some studies have found that constraining the use of satellites with incidence angles between 10° and 50° leads to more sensitive retrieval results (Small et al. 2016). One of the main limitations of GNSS-R, however, is that the likelihood of accurate SWC retrievals from GNSS-R observations decreases with increasing soil surface roughness. The footprint size of this technology, or first Fresnel zone, is in the order of tenths to hundreds of squared meters, depending on the elevation angle of the GNSS satellite, and the distance above the ground and the radiation pattern of the receiving antenna. The majority of GNSS-R alternatives in the literature have been assessed for the US Global Positioning System (GPS) constellation. However, its use could be extended to other GNSS, such as Galileo (Europe), GLONASS (Russia), and BeiDou (China).

A cost-effective GNSS-R approach is the GPS interferometric reflectometry (GPS-IR), which uses standard, commercial geodetic GPS antennas and receivers deployed in several networks around the globe. The number of units in these networks is rapidly increasing, and at present approximately 10,000 have their data publicly available in near real-time, several of them with long-term data records. For a typical antenna height of about 2 m, the footprint has a radius between 20 and 30 m. Soil moisture and vegetation water content are derived from the temporal changes in the signal-to-noise ratio (SNR) interferogram between the direct and reflected GPS signals. The phase of the SNR interferogram varies linearly with SWC, although additionally, the vegetation contribution to phase changes was found to be in the same order of magnitude at sites with VWC > 1 kg m^{-2}. Changes in the amplitude of the reflected GPS signal, however, are largely related to temporal changes in the vegetation, with the amplitude decreasing with increasing VWC. Therefore, some of the GPS-IR retrieval algorithms estimate first the vegetation conditions from the amplitude of the SNR interferogram, and then derive the SWC from the corrected phase. The accuracy of the GPS-IR surface SWC retrieval is ≈ 0.04 m^3 m^{-3} after taking into account the vegetation effects (Small et al. 2016; Larson 2016). This accuracy meets the target for satellite missions and is within the tolerance of in situ probes such as time-domain reflectometry and capacitance sensors.

Another ground-based alternative is to use sensors that have been specifically designed to measure the GPS reflections on the land. Over a 6-month period, Egido et al. (2012) evaluated the sensitivity of GNSS-R to SWC and VWC over a bare and vegetated agricultural area using a system at 25 m height, with three circular polarization antennas, one RHCP (right-hand circular polarization) uplooking and two (LHCP – left-hand circular polarization – and RHCP) downlooking, acquiring data sequentially. A sensitivity of 0.3 dB/SWC (%) and R = 0.76 was found if the LHCP downlooking antenna was used, whereas little sensitivity was found in the case of the RHCP antenna. Rodriguez-Alvarez et al. (2011) designed and

implemented the SMIGOL (Soil Moisture Interference Pattern GNSS Observations at L-band) reflectometer, which measures the power of the interference between the direct and reflected GPS signals. This approach, known as interference pattern technique (IPT), uses one V-pol antenna pointing at the horizon and is able to estimate the SWC within a $\approx$20 m radius at an accuracy <0.05 m^3 m^{-3} and at a spatial resolution of tenths of centimeters. The concept was later extended to dual-polarization, H- and V-pol (PSMIGOL; Alonso-Arroyo et al. 2014), and has also been successfully used for vegetation height, topography, water level, and snow thickness applications. The main limitation of these and any other stationary sensors is, however, their non-capability to provide spatially distributed SWC information over larger areas, if required. To circumvent this limitation, some GNSS-R instruments have been designed for airborne applications over land (e.g., Alonso-Arroyo et al. 2016; Motte et al. 2016).

An example which illustrates the potential of roving GNSS-R systems for agriculture is shown hereafter. The advantages of such a system over airborne platforms, which have been the alternative to stationary antennas for farm-scale applications, are evident: lower deployment cost, on-demand availability, and higher spatial resolution. Figure 9 (left) shows an overview of the tractor setup used during the field experiments conducted to evaluate this proof of concept, which was a first of its kind (Australian Grains Research and Development Corporation (GRDC), through funding to the project UMO-004 "On-the-go soil moisture monitoring using GPS signals during routine farming practices"). The experiment site was a rain fed winter barley paddock in North-West Victoria, Australia. Due to the large size of the farm, a focus area of 400 m (E-W) $\times$ 300 m (N-S) was selected. The GNSS-R sensor used is an improved version of the LARGO (Light Airborne Reflectometer for GNSS-R Observations), for which the sensitivity to SWC changes had been successfully tested in an airborne (Alonso-Arroyo et al. 2016) and a ground-based
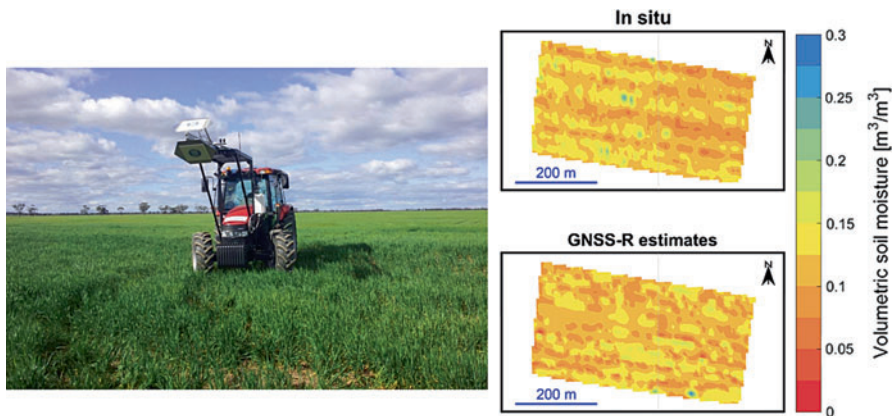
Fig. 9 (Left) Overview of the GNSS-R tractor setup used during the surveys conducted in North-West of Victoria, Australia. (Right) Maps showing the *in situ* and estimated volumetric SWC during one of the tractor surveys

configuration during the 2013–2014 GELOz experiments (GNSS-R experiments over land in Australia). The LARGO II sensor in Fig. 9 (left) consists of one RHCP uplooking and one LHCP downlooking, highly directive customized antennas at GPS L1 frequency. The antennas were installed at a 30° tilt from the horizontal and 2.75 m above the ground level. The GPS direct and reflected signals measured for all the satellites in view are stored internally every second. As the tractor surveys were conducted at a speed of 5 km h^{-1}, this translated into one acquisition every 1.4 m. The footprint size varied between 1 and 5 m^2, depending on the elevation of the GPS satellite. A series of auxiliary data sets were collected to gain knowledge of the in situ conditions at the farm and to be used for the validation and interpretation of the soil moisture retrievals. Optical and thermal sensors were mounted on the same frame as the LARGO II to derive crop properties, such as normalized difference vegetation index (NDVI) and temperature. Volumetric surface SWC was sampled every ≈ 15 m using EM sensors (Stevens Hydraprobe). Geo-located values of soil temperature, dielectric constant, and bulk electrical conductivity, and user-input crop data such as height and the presence of dew, were recorded as well.

The in situ and estimated SWC during one of the experiments is shown in Fig. 9 (right). The GNSS-R observations were filtered, and only GPS satellites with incidence angles between 10° and 50° were used in the retrieval algorithm. A simple forward model was used, in which the vegetation effect was modeled as an offset added to the bare soil contribution. Although the LARGO II instrument used has a 1 s measurement interval, the estimated SWC points were averaged at a coarser spatial resolution to reduce the noise inherent to the GNSS-R technique. A grid size of 10 m was found to be adequate, but it will depend on the speed of the tractor, and the position of the GPS satellites during the surveys. As there were no observations in some areas of the paddock, due to the geometry of the problem and the filtering of the data, the GNSS-R grid estimates were interpolated using the kriging method to obtain a full map of the focus area. No significant correlation between in situ and estimated SWC was found, due to the limited range of SWC conditions observed and the noise in the GNSS-R measurements. The spatial variation in SWC was, nevertheless, captured, and the probability distribution functions of both SWC data sets were similar, resulting in root-mean-square errors ≈0.04 m^3 m^{-3}. Although further experimental data is required to implement a robust retrieval algorithm, the use of this roving GNSS-R system has already proven to be an asset for farm-scale applications.

Nuclear Magnetic Resonance

Nuclear magnetic resonance (NMR) is a physical phenomenon that can yield molecular properties of matter by irradiating atomic nuclei, in a magnetic field, with electromagnetic radio waves (Blümich et al. 2014). NMR is particularly sensitive to the presence of protons ^{1}H and is therefore suited to investigate processes that involve water. When applied to the study of soil, NMR can be used to infer SWC, total porosity, and pore-size distribution and to quantify bound and producible fluid fractions.

Protons ^{1}H possess an intrinsic magnetic moment and angular momentum and consequently a nonzero spin (spin = ½). Under an external magnetic field of strength B_0, they will thus behave like small bar magnets that may orient parallel or antiparallel to the direction of $\mathbf{B_0}$, defining two energy levels (low E^- and high E^+, respectively) as illustrated in Fig. 10. The relative number (N) of nuclei in each spin state is described by the Boltzmann distribution:

$$\frac{N^+}{N^-} = e^{\left(-\frac{(E^+ - E^-)}{k_b T}\right)} \tag{15}$$

where k_b is the Boltzmann constant and T is the temperature in K.

In thermal equilibrium, the parallel state, more energetically favorable, is slightly more populated than the antiparallel state.

The rotational axis of the spinning nucleus is not oriented exactly parallel or antiparallel to the direction of $\mathbf{B_0}$. It exhibits a certain angle which causes precession, similarly to a spinning-top, around $\mathbf{B_0}$ at a frequency, called the Larmor or resonance frequency. The latter can be calculated with the following expression:

$$\nu_0 = \frac{(E^+ - E^-)}{h} = \frac{\gamma B_0}{2\pi} \tag{16}$$

where h is Planck's constant (expressed in J s), γ is the gyromagnetic ratio which is specific for each atomic nucleus (expressed in rad s^{-1} T^{-1}), and B_0 is the strength of the magnetic field (expressed in T). In a 1 Tesla field, the Larmor frequency of protons ^{1}H is 42.576 MHz.

The macroscopic magnetization, $\mathbf{M_0}$, of a sample is given by the sum of each spin vectors, as illustrated in Fig. 10. This magnetization can be used to infer the proton density in the sample submitted to $\mathbf{B_0}$. Assuming that water is the main source of ^{1}H protons in the investigated volume, proton density can be directly related to the water content.
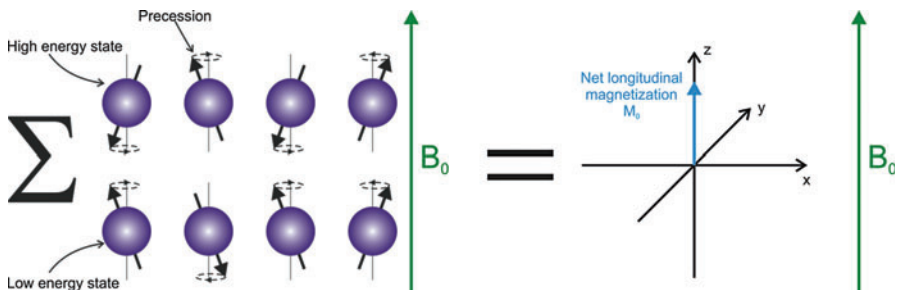
Fig. 10 Due to the slight difference of spin population in the two energy levels at thermal equilibrium, the sum of all the magnetic moments produces a macroscopic magnetization in the direction of $\mathbf{B_0}$, also known as the net longitudinal magnetization

The quantification of $\mathbf{M_0}$ is not possible as long as it points in the same direction as $\mathbf{B_0}$. In order to measure it, it is necessary to tip the magnetization away from its alignment with the external magnetic field. This is achieved by applying a radio-frequency (rf) magnetic impulse via a coil, at the Larmor frequency, that generates an oscillating magnetic field, $\mathbf{B_1}$, in the perpendicular plane to $\mathbf{B_0}$. The resulting tipped magnetization now oscillates at the Larmor frequency in the transverse plane to $\mathbf{B_0}$ generating an electrical field that can be detected by an antenna (generally the coil used to produce the excitation rf impulse). For a single pulse, the maximum intensity of the signal is recorded when the flip angle is 90° so that all the magnetization $\mathbf{M_0}$ is transferred into the orthogonal plane to $\mathbf{B_0}$.

At the end of the pulse, the nuclei relax and return to their equilibrium positions and the recorded signal decays. Under a homogeneous magnetic field $\mathbf{B_0}$, the response signal decays with a time constant T_2, called the transverse relaxation time, whereas in an inhomogeneous magnetic field, it decays with a generally smaller time constant T_2^*. In order to compensate for the effect of inhomogeneous magnetic field, it is possible to apply a series of 180° pulses after the excitation pulse in order to refocus spins that would have encountered a dephasing. This measurement sequence is known as Carr-Purcell-Meiboom-Gill (CPMG) echo train and is the standard way to estimate T_2 in inhomogeneous magnetic field environment. The time required to rebuild the magnetization along $\mathbf{B_0}$ is called the longitudinal relaxation time T_1 (with $T_1 > T_2 \geq T_2^*$).

The principle of NMR signal acquisition is illustrated in Fig. 11.

NMR Parameters

Two types of NMR parameters, particularly interesting in soil physics, can be determined from the impulse response signal: (1) the spin density and (2) the relaxation times.

Spin density (or proton density when focusing on ^{1}H atomic nuclei) represents the total number of spins present in the investigated volume and is directly proportional to the initial amplitude of the impulse response ($=S(0)$ in Fig. 11). By comparing the initial amplitude of the signal with the initial amplitude of a reference sample, soil water content or total porosity (in fully saturated conditions) can be estimated. Spin density is probably the most basic NMR parameter and can generally be measured with any NMR instrument (Blümich et al. 2014).

Relaxation times T_1 and T_2 are important parameters in NMR for material characterization and discrimination. In complex media, such as in soil, there is generally not a single T_1 or T_2 value characteristic of the whole sample, but rather distributions of T_1 and T_2 values. In porous media, during the acquisition of the signal, water molecules may encounter two different environments where relaxation of the signal may occur: the pore surface and the bulk fluid volume. Three NMR relaxation mechanisms influence T_1 or T_2 relaxation times: (1) bulk fluid relaxation, (2) relaxation by molecular diffusion in internal and external magnetic field gradients, and (3) grain surface relaxation. Bulk fluid relaxation is the intrinsic relaxation property of the fluid. It can generally be neglected in porous media (because much
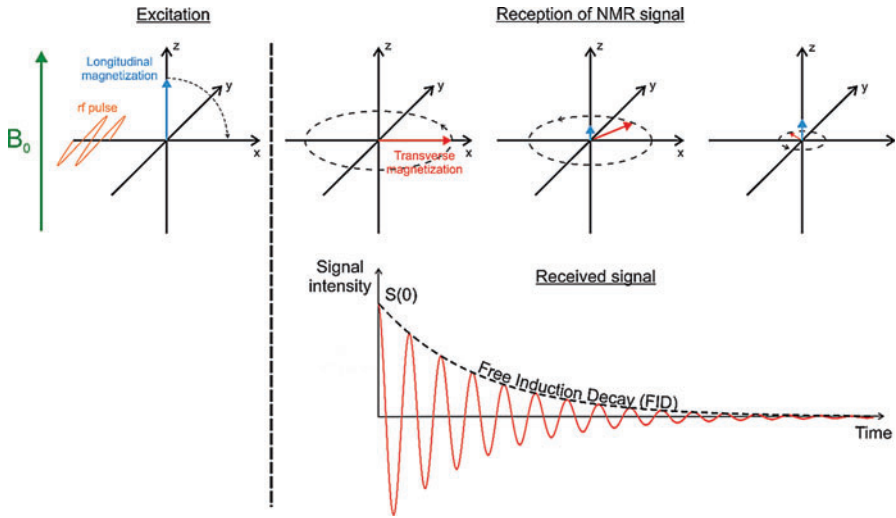
Fig. 11 During the excitation phase, the magnetization is tipped away from the direction of $\mathbf{B_0}$ by a rf pulse applied at the resonance frequency. If the amplitude and duration of the pulse is correctly adjusted, all the magnetization can be rotated in the x-y plane. The resulting transverse magnetization precesses now in the x-y plane at the Larmor frequency and generates a signal that can be detected by an antenna. The decay of the signal is due to two types of relaxation: (1) the realignment of spins along $\mathbf{B_0}$, also called longitudinal or T_1 relaxation (regrow of blue arrow), and (2) the loss of synchronization of the spins due to spin-spin interactions and magnetic field inhomogeneity, also called T_2^* relaxation (decrease of red arrow)

slower than the two others relaxation mechanisms). The motion of water molecules by diffusion in magnetic field gradients during the measurement, meaning that water molecules may experience regions with different Larmor frequencies, induces a dephasing of spins which is responsible of T_2 relaxation. Grain surface relaxation is generally the dominant relaxation mechanism in porous media. It occurs when water molecules diffuse close to paramagnetic impurities at the pore wall or grain surface. Water molecules in large pores collide less frequently with pore walls and consequently relax slower than water molecules in small pores so that, in saturated media and under certain conditions (not detailed here), T_1 or T_2 distributions may mimic pore-size distribution (Kenyon et al. 1995).

In unsaturated media, T_2 distribution appears to be rather a measure of the distribution of the water within the pore space at a specific degree of saturation than a measure of the pore-size distribution as shown by Costabel and Yaramanci (2011).

Available in Situ NMR Sensors
Currently, three types of NMR sensors can be used in situ to measure SWC. Their implementation on the field is schematized in Fig. 12:
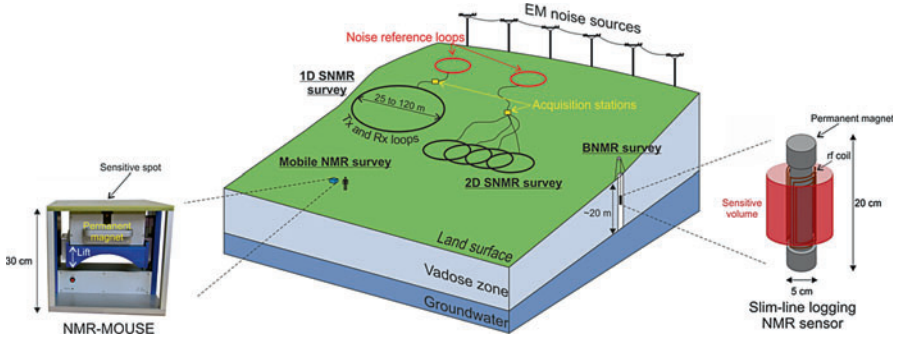
Fig. 12 Possible in situ applications of NMR for SWC measurements. Three methods are illustrated, each having its own advantages. Mobile NMR sensors such as the NMR-MOUSE developed by Magritek Ltd. offer a way to probe the very first centimeters of soil with a high vertical resolution. BNMR sensors, like the slim-line logging sensor schematized here (modified from Perlo et al. 2013) and developed by the RWTH Aachen, are particularly suited to quantify SWC in the vadose zone with a vertical resolution of 10 cm (Behroozmand et al. 2015). SNMR allows to investigate water content from shallow horizons to more than 100 m depth without requiring the drilling of boreholes (scheme modified from Vista Clara Inc 2016). All methods presented are very sensitive to ambient EM noise and particular precautions (such as the deployment of noise reference loops in SNMR) must be taken to reduce its effect on the data quality

1. Mobile low-field NMR sensors (single-sided NMR) such as the NMR-MOUSE (Magritek Ltd.) that allows to investigate water content of topsoil down to a maximum depth of 2.5 cm (Blümich et al. 2014). The device is based on the principle of "inside-out" NMR and is composed of a permanent U-shape magnet generating a magnetic gradient perpendicular to the surface (Blümich et al. 1998). A rf coil, mounted above the magnet, is used to excite the spins and receive the NMR signal coming from a sensitive volume whose thickness (i.e., resolution) ranges from 5 to 100 μm depending on the device model. The magnet is mounted on a lift so that it is possible to acquire one-dimensional profiles.

2. Borehole NMR (BNMR) sensors were initially developed for the characterization of petroleum resources. Unfortunately, these sensors are not suited for shallow measurements of SWC due to their dimension that largely exceeds the classical size of wells in this depth range. To overcome that, slim-line logging tools were developed (e.g., Perlo et al. 2013; Walsh et al. 2013). The principle of measurement is similar to the NMR-MOUSE except that the sensitive zone is, in this case, a thin cylindrical region around the outside of the borehole.

3. Surface NMR (SNMR). The main difference of SNMR compared to other NMR methods is the use of the earth magnetic field instead of the large magnetic field created by magnets. The rf signal used to excite the spins is generated by a wire loop laid down on the ground (Legchenko et al. 2002). The same loop is also used to receive the NMR signal after the excitation. The depth of investigation of this method depends on the loop size and site-specific conditions, such as the presence of electrically conductive layers below the setup, but usually ranges from 40 to

120 m (Legchenko et al. 2011). SNMR was initially designed for 1-D sounding (in that case, the term magnetic resonance sounding (MRS) is generally employed), but 2-D and even 3-D applications of the method are possible (e.g., Hertrich et al. 2007).

We refer the interested reader to the review paper of Behroozmand et al. (2015) for more information about the introduced methods.

Soil water content, after the collection of a sample, can also be measured in laboratory using various NMR tools. Among them, magnetic resonance imaging (MRI), a technique commonly used in medicine, holds particular interest because it allows the visualization in 2-D or in 3-D of SWC with a very high resolution (e.g., Pohlmeier et al. 2008; Merz et al. 2016).

NMR techniques have demonstrated for years their usefulness to quantify water content at great depths (e.g., BNMR logging tools in petroleum industry). However, the development of NMR sensors to investigate SWC at shallower depth with high spatial resolution is relatively recent and improvements are still required in order for these sensors to be routinely used in that scope. Among possible optimizations, one can point out the reduction of the dead time (= time between excitation and signal acquisition) and/or echo time in order to capture fast-decaying signals (possibly caused by fine pore materials or the presence of paramagnetic impurities) and the development of new processing tools to reduce the effect of EM noise and increase the signal-to-noise ratio.

Summary and Outlook

Soil water content is a key variable for understanding and modeling ecohydrological processes. In this chapter, we reviewed the state of the art with respect to the spatiotemporal characterization of SWC from point to field scale using ground-based techniques. The number of SWC measurement methods has significantly increased over the last years, in particular with the emergence of novel techniques such as cosmic-ray neutron probes, navigation satellite system reflectometry, and nuclear magnetic resonance. Large improvements have also been made in order to fully exploit the information contained in soil moisture data by using data assimilation techniques, more sophisticated data processing approaches, and inversion schemes (e.g., coupled hydrogeophysical inversion, full-waveform analysis for GPR). More accurate instruments (e.g., better signal-to-noise ratio, smaller instrument drift for EMI) have also been developed during the last decade. There is still a need for soil moisture data with higher temporal and spatial resolution, which is particularly useful for observing ecohydrological processes. Finally, combination of different measurement techniques (such as ERT and EMI or active and passive microwave systems) with complementary characteristics might be an interesting avenue to further explore.

References

H. Abdu, D.A. Robinson, M. Seyfried, S.B. Jones, Geophysical imaging of watershed subsurface patterns and prediction of soil texture and water holding capacity. Water Resour. Res. **44**(4), W00D18 (2008)

S.A. al Hagrey, Electrical resistivity imaging of tree trunks. Near Surf. Geophys. **4**, 179–187 (2006)

A. Alonso-Arroyo, A. Camps, A. Monerris, C. Rüdiger, J.P. Walker, A. Aguasca, G. Forte, H. Park, D. Pascual, R. Onrubia, Dual-polarization GNSS-R interference pattern technique for soil moisture mapping. IEEE J. Sel. Top. Appl. Earth Obs. Remote Sens. **7**(5), 1533–1544 (2014)

A. Alonso-Arroyo, A. Camps, A. Monerris, C. Rüdiger, J.P. Walker, R. Onrubia, J. Querol, H. Park, D. Pascual, On the correlation between GNSS reflectometry and L-band radiometry. IEEE J. Sel. Top. Appl. Earth Obs. Remote Sens. **9**(12), 5862–5879 (2016)

D. Altdorff, M. Bechtold, J. van der Kruk, H. Vereecken, J.A. Huisman, Mapping peat layer properties with multi-coil offset electromagnetic induction and laser scanning elevation data. Geoderma **261**, 178–189 (2016)

F. André, F. Jonard, M. Jonard, S. Lambot, In situ characterization of forest litter using ground-penetrating radar. J. Geophys. Res. Biogeo. **121**(3), 879–894 (2016)

M. Andreasen, K.H. Jensen, M. Zreda, D. Desilets, H. Bogena, M.C. Looms, Modeling cosmic ray neutron field measurements. Water Resour. Res. **52**(8), 6451–6471 (2016)

U. Aqeel-ur-Rehman, A.Z. Abbasi, N. Islam, Z.A. Shaikh, A review of wireless sensors and networks' applications in agriculture. Comput. Stand. Interfaces **36**(2), 263–270 (2014)

G.E. Archie, The electrical resistivity log as an aid in determining some reservoir characteristics. Trans. AIME **146**, 54–61 (1942)

R. Baatz, H. Bogena, H.-J. Hendricks Franssen, J.A. Huisman, C. Montzka, H. Vereecken, An empirical vegetation correction for soil water content quantification using cosmic ray probes. Water Resour. Res. **51**(4), 2030–2046 (2015)

O. Banton, M.K. Seguin, M.A. Cimon, Mapping field-scale physical properties of soil with electrical resistivity. Soil Sci. Soc. Am. J. **61**, 1010–1017 (1997)

G. Baroni, S. Oswald, A scaling approach for the assessment of biomass changes and rainfall interception using cosmic-ray neutron sensing. J. Hydrol. **525**, 264–276 (2015)

A.A. Behroozmand, K. Keating, E. Auken, A review of the principles and applications of the NMR technique for near-surface characterization. Surv. Geophys. **36**, 27–85 (2015)

A. Binley, R3t (version 1.8), Lancaster University (2013) [Logiciel]. Repéré à http://www.es.lancs.ac.uk/people/amb/Freeware/R3t/R3t.htm

J.R. Birchak, C.G. Gardner, J.E. Hipp, J.M. Victor, High dielectric constant microwave probes for sensing soil moisture. Proc. IEEE **62**, 93–98 (1974)

S. Bircher, N. Skou, K. Jensen, J. Walker, L. Rasmussen, A soil moisture and temperature network for SMOS validation in Western Denmark. Hydrol. Earth Syst. Sci. **16**, 1445–1463 (2012)

B. Blümich, P. Blümler, G. Eidmann, A. Guthausen, R. Haken, U. Schmitz, K. Saito, G. Zimmer, The NMR-mouse: Construction, excitation, and applications. Magn. Reson. Imaging **16**, 479–484 (1998)

B. Blümich, S. Haber-Pohlmeier, W. Zia, *Compact NMR* (Walter de Gruyter GmbH, Berlin., 276 pp, 2014)

H. Bogena, M. Herbst, J.A. Huisman, U. Rosenbaum, A. Weuthen, H. Vereecken, Potential of wireless sensor networks for measuring soil water content variability. Vadose Zone J. **9**(4), 1002–1013 (2010)

H. Bogena, R. Kunkel, E. Krüger, S. Zacharias, T. Pütz, M. Schwank, O. Bens, E. Borg, A. Brauer, P. Dietrich, I. Hajnsek, H. Kunstmann, J.-C. Munch, H. Papen, E. Priesack, H.P. Schmid, U. Wollschläger, H. Vereecken, TERENO – Long-term monitoring network for terrestrial research. Hydrol. Wasserbewirtsch. **56**(3), 138–143 (2012)

H. Bogena, J.A. Huisman, R. Baatz, H.-J. Hendricks Franssen, H. Vereecken, Accuracy of the cosmic-ray soil water content probe in humid Forest ecosystems: The worst case scenario. Water Resour. Res. **49**(9), 5778–5791 (2013)

H. Bogena, J.A. Huisman, A. Güntner, C. Hübner, J. Kusche, F. Jonard, S. Vey, H. Vereecken, Emerging methods for non-invasive sensing of soil moisture dynamics from field to catchment scale: A review. WIREs Water **2**(6), 635–647 (2015a)

S. Busch, J. van der Kruk, J. Bikowski, H. Vereecken, Quantitative conductivity and permittivity estimation using full-waveform inversion of onground GPR data. Geophysics **77**(6), H79–H91 (2012)

G. Calamita, A. Perrone, L. Brocca, B. Onorati, S. Manfreda, Field test of a multi-frequency electromagnetic induction sensor for soil moisture monitoring in southern Italy test sites. J. Hydrol. **529**, 316–329 (2015)

R.B. Campbell, Change of electrical conductivity with temperature and the relation of osmotic pressure to electrical conductivity and ion concentration for soil extracts. Soil Sci. Soc. Am. J. **13**, 66–69 (1949)

G. Cassiani, J. Boaga, D. Vanella, M.T. Perri, S. Consoli, Monitoring and modelling of soil-plant interactions: The joint use of ERT, sap flow and eddy covariance data to characterize the volume of an orange tree root zone. Hydrol. Earth Syst. Sci. **19**(5), 2213–2225 (2015)

D. Caterina, J. Beaujean, T. Robert, F. Nguyen, A comparison study of different image appraisal tools for electrical resistivity tomography. Near Surf. Geophys. **11**, 639–657 (2013)

B.B. Chrisman, M. Zreda, Quantifying mesoscale soil moisture with the cosmic-ray rover. Hydrol. Earth Syst. Sci. **17**(12), 5097–5108 (2013)

E.J. Coopersmith, M.H. Cosh, C.S.T. Daughtry, Field-scale moisture estimates using COSMOS sensors: A validation study with temporary networks and leaf-area indices. J. Hydrol. **519**(Part A), 637–643 (2014)

D.L. Corwin, S.M. Lesch, Application of soil electrical conductivity to precision agriculture: Theory, principles, and guidelines. Agron. J. **95**(3), 455–471 (2003)

S. Costabel, U. Yaramanci, Relative hydraulic conductivity and effective saturation from earth's field nuclear magnetic resonance-a method for assessing the vadose zone. Near Surf. Geophys. **9**, 155–167 (2011)

J. Davis, A. Annan, Ground-penetrating radar for high-resolution mapping of soil and rock stratigraphy. Geophys. Prospect. **37**, 531–551 (1989)

C. de Groot-Hedlin, S. Constable, Occam's inversion to generate smooth, two dimensional models form magnetotelluric data. Geophysics **55**, 1613–1624 (1990)

P. de Rosnay, J.-C. Calvet, Y. Kerr, J.-P. Wigneron, F. Lemaître, M.-J. Escorihuela, J. Muñoz Sabater, K. Saleh, J. Barrié, G. Bouhours, L. Coret, G. Cherel, G. Dedieu, R. Durbe, F.N.E. Dine, F. Froissard, J. Hoedjes, A. Kruszewski, F. Lavenu, D. Suquia, P. Waldteufel, SMOSREX: A long term field campaign experiment for soil moisture and land surface processes remote sensing. Remote Sens. Environ. **102**, 377 (2006)

D. Desilets, M. Zreda, T.P.A. Ferre, Nature's neutron probe: Land surface hydrology at an elusive scale with cosmic-rays. Water Resour. Res. **46**, W11505 (2010)

M.C. Dobson, F.T. Ulaby, M.T. Hallikainen, M.A. El-Rayes, Microwave dielectric behavior of wet soil-part II: Dielectric mixing models. IEEE Trans. Geosci. Remote Sens. **23**(1), 35–46 (1985)

J.N. Dong, T.E. Ochsner, M. Zreda, M.H. Cosh, C.B. Zou, Calibration and validation of the COSMOS rover for surface soil moisture measurement. Vadose Zone J. **13**(4) (2014)

L.S. Edwards, A modified pseudosection for resistivity and IP. Geophysics **42**(5), 1020–1036 (1977)

A. Egido, M. Caparrini, G. Ruffini, S. Paloscia, E. Santi, L. Guerriero, N. Pierdicca, N. Floury, Global navigation satellite systems reflectometry as a remote sensing tool for agriculture. Remote Sens. **4**, 2356–2372 (2012)

J.R. Ernst, H. Maurer, A.G. Green, K. Holliger, Full-waveform inversion of crosshole radar data based on 2-D finite-difference time-domain solutions of Maxwell's equations. IEEE Trans. Geosci. Remote Sens. **45**(9), 2807–2828 (2007)

J.S. Famiglietti, D.R. Ryu, A.A. Berg, M. Rodell, T.J. Jackson, Field observations of soil moisture variability across scales. Water Resour. Res. **44**(1), W01423, 1–16 (2008)

T.E. Franz, T. Wang, W. Avery, C. Finkenbiner, L. Brocca, Combined analysis of soil moisture measurements from roving and fixed cosmic ray neutron probes for multiscale real-time monitoring. Geophys. Res. Lett. **42**, 3389–3396 (2015)

S. Friedel, Resolution, stability and efficiency of resistivity tomography estimated from a generalized inverse approach. Geophys. J. Int. **153**, 305–316 (2003)

H. Fuchs, Effects of biomass on soil moisture measurements using cosmic-ray neutron probes. Master Thesis, Radboud University and University of Duisburg-Essen, 59 pp. (2016)

S. Garré, M. Javaux, J. Vanderborght, L. Pages, H. Vereecken, Three-dimensional electrical resistivity tomography to monitor root zone water dynamics. Vadose Zone J. **10**(1), 412–424 (2011)

S. Garré, T. Günther, J. Diels, J. Vanderborght, Evaluating experimental design of ERT for soil moisture monitoring in contour hedgerow intercropping systems. Vadose Zone J. **11**(4), 1–14 (2012)

S. Garré, I. Coteur, C. Wongleecharoen, T. Kongkaew, J. Diels, J. Vanderborght, Non-invasive monitoring of soil water dynamics in mixed cropping systems: A case-study in Ratchaburi province, Thailand. Vadose Zone J. **12**(2), 1–12 (2013)

M. Guglielmetti, M. Schwank, C. Mätzler, C. Oberdörster, J. Vanderborght, H. Flühler, FOSMEX: Forest soil moisture experiments with microwave radiometry. IEEE Trans. Geosci. Remote Sens. **46**(3), 727 (2008)

T. Günther, Inversion Methods and Resolution Analysis for the 2D/3D Reconstruction of Resistivity Structures from DC Measurements, PhD Thesis, University of Mining and Technology, Freiberg (2004)

N. Güting, A. Klotzsche, J. van der Kruk, J. Vanderborght, H. Vereecken, A. Englert, Imaging and characterization of facies heterogeneity in an alluvial aquifer using GPR full-waveform inversion and cone penetration tests. J. Hydrol. **524**, 680–695 (2015)

I. Heidbüchel, A. Güntner, T. Blume, Use of cosmic-ray neutron sensors for soil moisture monitoring in forests. Hydrol. Earth Syst. Sci. **20**(3), 1269–1288 (2016)

T. Hermans, E. Oware, J. Caers, Direct prediction of spatially and temporally varying physical properties from time-lapse electrical resistance data. Water Resour. Res. **52**, 7262–7283 (2016)

M. Hertrich, M. Braun, T. Gunther, A.G. Green, U. Yaramanci, Surface nuclear magnetic resonance tomography. IEEE Trans. Geosci. Remote Sens. **45**, 3752–3759 (2007)

A.C. Hinnell, T.P.A. Ferré, J.A. Vrugt, J.A. Huisman, S. Moysey, J. Rings, M.B. Kowalsky, Improved extraction of hydrologic information from geophysical data through coupled hydrogeophysical inversion. Water Resour. Res. **46**, W00D40 (2010)

J.A. Huisman, S.S. Hubbard, J.D. Redman, A.P. Annan, Measuring soil water content with ground penetrating radar, A review. Vadose Zone J. **2**(4), 476–491 (2003)

R.B. Jana, A. Ershadi, M.F. McCabe, Examining the relationship between intermediate scale soil moisture and terrestrial evaporation within a semi-arid grassland. Hydrol. Earth Syst. Sci. **20**(9), 3987–4004 (2016)

R. Jin, X. Li, B. Yan, X. Li, W. Luo, M. Ma, J. Guo, J. Kang, Z. Zhu, S. Zhao, A nested ecohydrological wireless sensor network for capturing the surface heterogeneity in the midstream areas of the Heihe River Basin, China. IEEE Geosci. Remote Sens. Lett. **11**(11), 2015–2019 (2014)

S.G. Jin, E. Cardellach, F. Xie, *GNSS Remote Sensing: Theory, Methods and Applications* (Springer, Heidelberg., 276 pp, 2014)

H. M. Jol (ed.), *Ground Penetrating Radar: Theory and Applications* (Elsevier Science, Amsterdam., 524 pp, 2009)

F. Jonard, F. André, Q. Ponette, C. Vincke, M. Jonard, Sap flux density and stomatal conductance of European beech and common oak trees in pure and mixed stands during the summer drought of 2003. J. Hydrol. **409**, 371–381 (2011a)

F. Jonard, L. Weihermüller, K.Z. Jadoon, M. Schwank, H. Vereecken, S. Lambot, Mapping field-scale soil moisture with L-band radiometer and ground-penetrating radar over bare soil. IEEE Trans. Geosci. Remote Sens. **49**(8), 2863–2875 (2011b)

F. Jonard, L. Weihermüller, H. Vereecken, S. Lambot, Accounting for soil surface roughness in the inversion of ultrawideband off-ground GPR signal for soil moisture retrieval. Geophysics **77**(1), H1–H7 (2012)

F. Jonard, M. Mahmoudzadeh, C. Roisin, L. Weihermüller, F. André, J. Minet, H. Vereecken, S. Lambot, Characterization of tillage effects on the spatial variation of soil properties using ground-penetrating radar and electromagnetic induction. Geoderma **207–208**, 310–322 (2013)

F. Jonard, L. Weihermüller, M. Schwank, K.Z. Jadoon, H. Vereecken, S. Lambot, Estimation of hydraulic properties of a sandy soil using ground-based active and passive microwave remote sensing. IEEE Trans. Geosci. Remote Sens. **53**(6), 3095–3109 (2015)

A. Kemna, *Tomographic Inversion of Complex Resistivity-Theory and Application* (Ruhr-Universität, Bochum, 2000)

B. Kenyon, R. Kleinberg, C. Straley, G. Gubelin, C. Morriss, Nuclear magnetic resonance imaging-technology for the 21st century. Oilfield Rev **7**, 19–33 (1995)

A. Klotzsche, J. van der Kruk, G. Meles, H. Vereecken, Crosshole GPR full-waveform inversion of waveguides acting as preferential flow paths within aquifer systems. Geophysics **77**(4), H57–H62 (2012)

A. Klotzsche, J. van der Kruk, N. Linde, J. Doetsch, H. Vereecken, 3-D characterization of high-permeability zones in a gravel aquifer using 2-D crosshole GPR full-waveform inversion and waveguide detection. Geophys. J. Int. **195**(2), 932–944 (2013)

A. Klotzsche, J. van der Kruk, J. Bradford, H. Vereecken, Detection of spatially limited high porous layers using crosshole GPR signal analysis and full-waveform inversion. Water Resour. Res. **50**(8), 6966–6985 (2014)

M. Köhli, M. Schrön, M. Zreda, U. Schmidt, P. Dietrich, S. Zacharias, Footprint characteristics revised for field-scale soil moisture monitoring with cosmic-ray neutrons. Water Resour. Res. **51**, 5772–5790 (2015)

S. Lambot, E.C. Slob, I. van den Bosch, B. Stockbroeckx, M. Vanclooster, Modeling of ground-penetrating radar for accurate characterization of subsurface electric properties. IEEE Trans. Geosci. Remote Sens. **42**(11), 2555–2568 (2004)

K.M. Larson, GPS interferometric reflectometry: Applications to surface soil moisture, snow depth, and vegetation water content in the western United States. WIREs Water **3**(6), 775 (2016)

F. Lavoué, J. van der Kruk, J. Rings, F. André, D. Moghadas, J.A. Huisman, S. Lambot, L. Weihermüller, J. Vanderborght, H. Vereecken, Electromagnetic induction calibration using apparent electrical conductivity modelling based on electrical resistivity tomography. Near Surf. Geophys. **8**(6), 553–561 (2010)

H. Lawrence, J.-P. Wigneron, P. Richaume, N. Novello, J. Grant, A. Mialon, A. Al Bitar, O. Merlin, D. Guyon, D. Leroux, S. Bircher, Y. Kerr, Comparison between SMOS vegetation optical depth products and MODIS vegetation indices over crop zones of the USA. Remote Sens. Environ. **140**, 396 (2014)

A. Legchenko, J.-M. Baltassat, A. Beauce, J. Bernard, Nuclear magnetic resonance as a geophysical tool for hydrogeologists. J. Appl. Geophys. **50**(1–2), 21–46 (2002)

A. Legchenko, M. Descloitres, C. Vincent, H. Guyard, S. Garambois, K. Chalikakis, M. Ezersky, Three-dimensional magnetic resonance imaging for groundwater. New J. Phys. **13**, 025022 (2011)

J. Lemmetyinen, M. Schwank, K. Rautiainen, A. Kontu, T. Parkkinen, C. Mätzler, A. Wiesmann, U. Wegmüller, P. Toose, A. Roy, J. Pulliainen, Snow density and ground permittivity retrieved from L-band radiometry: Application to experimental data. Remote Sens. Environ. **180**, 377 (2016)

M.H. Loke, R.D. Barker, Rapid least-squares inversion of apparent resistivity pseudosections by a quasi-Newton method. Geophys. Prospect. **44**, 131–152 (1996)

R. Ma, A. McBratney, B. Whelan, B. Minasny, M. Short, Comparing temperature correction models for soil electrical conductivity measurement. Precis. Agric. **12**, 55–66 (2011)

L. Marescot, M.H. Loke, D. Chapellier, R. Delaloye, C. Lambiel, E. Reynard, Assessing reliability of 2D resistivity imaging in mountain permafrost studies using the depth of investigation index method. Near Surf. Geophys. **1**(2), 57–67 (2003)

E. Martini, U. Werban, S. Zacharias, M. Pohle, P. Dietrich, U. Wollschläger, Repeated electromagnetic induction measurements for mapping soil moisture at the field scale: Validation with data from a wireless soil moisture monitoring network. Hydrol. Earth Syst. Sci. **21**(1), 495–513 (2017)

J.D. McNeill, *Electromagnetic Terrain Conductivity Measurement at Low Induction Numbers, Technical Note TN-6* (Geonics Ltd., Mississauga, 1980)

G.A. Meles, J. van der Kruk, S.A. Greenhalgh, J.R. Ernst, H. Maurer, A.G. Green, A. New Vector, Waveform inversion algorithm for simultaneous updating of conductivity and permittivity parameters from combination Crosshole/borehole-to-surface GPR data. IEEE Trans. Geosci. Remote Sens. **48**(12), 4329–4329 (2010)

S. Merz, A. Pohlmeier, B.J. Balcom, R. Enjilela, H. Vereecken, Drying of a natural soil under evaporative conditions: A comparison of different magnetic resonance methods. Appl. Magn. Reson. **47**, 121–138 (2016)

A. Mester, J. van der Kruk, E. Zimmermann, H. Vereecken, Quantitative two-layer conductivity inversion of multi-configuration electromagnetic induction measurements. Vadose Zone J. **10**(4), 1319–1330 (2011)

D. Michot, Y. Benderitter, A. Dorigny, B. Nicoullaud, D. King, A. Tabbagh, Spatial and temporal monitoring of soil water content with an irrigated corn crop cover using surface electrical resistivity tomography. Water Resour. Res. **39**, SBH 14 (2003)

J. Minet, P. Bogaert, M. Vanclooster, S. Lambot, Validation of ground penetrating radar full-waveform inversion for field scale soil moisture mapping. J. Hydrol. **424–425**, 112–123 (2012)

V.L. Mironov, L.G. Kosolapova, S.V. Fomin, Physically and Mineralogically based spectroscopic dielectric model for moist soils. IEEE Trans. Geosci. Remote Sens. **47**(7), 2059 (2009)

T. Mo, B.J. Choudhury, T.J. Schmugge, J.R. Wang, T.J. Jackson, A model for microwave emission from vegetation-covered fields. J. Geophys. Res. **87**, 11229 (1982)

E. Motte, M. Zribi, P. Fanise, A. Egido, J. Darrozes, A. Al-Yaari, N. Baghdadi, F. Baup, S. Dayau, R. Fieuzal, P.-L. Frison, D. Guyon, J.-P. Wigneron, GLORI: A GNSS-R dual polarization airborne instrument for land surface monitoring. Sensors **16**(5), 732 (2016)

D.W. Oldenburg, Y. Li, Estimating depth of investigation in DC resistivity and IP surveys. Geophysics **64**, 403–416 (1999)

J. Perlo, E. Danieli, J. Perlo, B. Blümich, F. Casanova, Optimized slim-line logging NMR tool to measure soil moisture in situ. J. Magn. Reson. **233**, 74–79 (2013)

A. Pohlmeier, A. Oros-Peusquens, M. Javaux, M. Menzel, J. Vanderborght, J. Kaffanke, S. Romanzetti, J. Lindenmair, H. Vereecken, N. Shah, Changes in soil water content resulting from root uptake monitored by magnetic resonance imaging. Vadose Zone J. **7**, 1010–1017 (2008)

K. Rautiainen, J. Lemmetyinen, M. Schwank, A. Kontu, C.B. Ménard, C. Mätzler, M. Drusch, A. Wiesmann, J. Ikonen, J. Pulliainen, Detection of soil freezing from L-band passive microwave observations. Remote Sens. Environ. **147**, 206 (2014)

A. Revil, P.W.J. Glover, Nature of surface electrical conductivity in natural sands, sandstones, and clays. Geophys. Res. Lett. **25**, 691–694 (1998)

J.D. Rhoades, N.A. Manteghi, P.J. Shouse, W.J. Alves, Soil electrical conductivity and soil salinity: New formulations and calibrations. Soil Sci. Soc. Am. J. **53**, 433–439 (1989)

T. Robert, A. Dassargues, S. Brouyère, O. Kaufmann, V. Hallet, F. Nguyen, Assessing the contribution of electrical resistivity tomography (ERT) and self-potential (SP) methods for a water well drilling program in fractured/karstified limestones. J. Appl. Geophys. **75**(1), 42–53 (2011)

D.A. Robinson, S.B. Jones, J.M. Wraith, D. Or, S.P. Friedman, A review of advances in dielectric and electrical conductivity measurement in soils using time domain reflectometry. Vadose Zone J. **2**, 444–475 (2003)

D.A. Robinson, C.S. Campbell, J.W. Hopmans, B.K. Hornbuckle, S.B. Jones, R. Knight, F. Ogden, J. Selker, O. Wendroth, Soil moisture measurement for ecological and hydrological watershed-scale observatories: A review. Vadose Zone J. **7**(1), 358–389 (2008)

D.A. Robinson, I. Lebron, B. Kocar, K. Phan, M. Sampson, N. Crook, S. Fendorf, Time-lapse geophysical imaging of soil moisture dynamics in tropical deltaic soils: An aid to interpreting hydrological and geochemical processes. Water Resour. Res. **45**, W00D32 (2009)

D.A. Robinson, H. Abdu, I. Lebron, S.B. Jones, Imaging of hill-slope soil moisture wetting patterns in a semi-arid oak savanna catchment using time-lapse electromagnetic induction. J. Hydrol. **416**, 39–49 (2012)

N. Rodriguez-Alvarez, X. Bosch-Lluis, A. Camps, A. Aguasca, M. Vall-llossera, E. Valencia, I. Ramos-Perez, H. Park, Review of crop growth and soil moisture monitoring from a ground-based instrument implementing the interference pattern GNSS-R technique. Radio Sci. **46**, RS0C03 (2011)

U. Rosenbaum, H. Bogena, M. Herbst, J.A. Huisman, T.J. Peterson, A. Weuthen, A. Western, H. Vereecken, Seasonal and event dynamics of spatial soil moisture patterns at the small catchment scale. Water Resour. Res. **48**(10), W10544 (2012)

K. Roth, R. Schulin, H. Flühler, W. Attinger, Calibration of time-domain reflectometry for water-content measurement using a composite dielectric approach. Water Resour. Res. **26**(10), 2267–2273 (1990)

S. Rudolph, J. van der Kruk, C.v. Hebel, M. Ali, M. Herbst, C. Montzka, S. Patzold, D.A. Robinson, H. Vereecken, L. Weihermuller, Linking satellite derived LAI patterns with subsoil heterogeneity using large-scale ground-based electromagnetic induction measurements. Geoderma **241**, 262–271 (2015)

A. Samouelian, I. Cousin, A. Tabbagh, A. Bruand, G. Richard, Electrical resistivity survey in soil science: A review. Soil Tillage Res. **83**, 173–193 (2005)

T. Schmugge, Remote sensing of soil moisture. in *Encyclopedia of Hydrological Forecasting*, ed. by M.G. Anderson, T. Burt (Wiley., Chichester/London, 101–124 1985)

M. Schwank, A. Wiesmann, C. Werner, C. Mätzler, D. Weber, A. Murk, I. Völksch, U. Wegmüller, ELBARA II, an L-band radiometer system for soil moisture research. Sensors MDPI **10**, 584 (2010)

M. Schwank, J.-P. Wigneron, E. Lopez-Baeza, I. Völksch, C. Mätzler, Y. Kerr, L-band radiative properties of vine vegetation at the SMOS Cal/Val site MELBEX III. IEEE Trans. Geosci. Remote Sens. **50**(5), 1587 (2012)

S.I. Seneviratne, D. Luthi, M. Litschi, C. Schar, Land-atmosphere coupling and climate change in Europe. Nature **443**(7108), 205–209 (2006)

S.I. Seneviratne, T. Corti, E.L. Davin, M. Hirschi, E.B. Jaeger, I. Lehner, B. Orlowsky, A.J. Teuling, Investigating soil moisture-climate interactions in a changing climate: A review. Earth Sci. Rev. **99**(3–4), 125–161 (2010)

K.R. Sheets, J.M.H. Hendrickx, Noninvasive soil water content measurement using electromagnetic induction. Water Resour. Res. **31**(10), 2401–2409 (1995)

E.E. Small, K.M. Larson, C.C. Chew, J. Dong, T.E. Ochsner, Validation of GPS-IR soil moisture retrievals: Comparison of different algorithms to remove vegetation effects. IEEE J. Sel. Top. Appl. Earth Obs. Remote Sens. **9**(10), 4759–4770 (2016)

C.M. Steelman, A.L. Endres, Comparison of petrophysical relationships for soil moisture estimation using GPR ground waves. Vadose Zone J. **10**, 270–285 (2011)

K.A. Sudduth, N.R. Kitchen, W.J. Wiebold, W.D. Batchelor, G.A. Bollero, D.G. Bullock, D.E. Clay, H.L. Palm, F.J. Pierce, R.T. Schuler, K.D. Thelen, Relating apparent electrical conductivity to soil properties across the north-central USA. Comput. Electron. Agric. **46**(1–3), 263–283 (2005)

M. Temimi, T. Lakhankar, X. Zhan, M.H. Cosh, N. Krakauer, A. Fares, V. Kelly, R. Khanbilvardi, L. Kumassi, Soil moisture retrieval using ground-based L-band passive microwave observations in northeastern USA. Vadose Zone J. **13**(3), 1–10 (2014)

G.C. Topp, J.L. Davis, A.P. Annan, Electromagnetic determination of soil-water content – Measurements in coaxial transmission-lines. Water Resour. Res. **16**(3), 574–582 (1980)

H. Vereecken, J.A. Huisman, H. Bogena, J. Vanderborght, J.A. Vrugt, J.W. Hopmans, On the value of soil moisture measurements in vadose zone hydrology: A review. Water Resour. Res. **44**(21), W00D06 (2008)

Vista Clara Inc. GMR (2016), http://www.vista-clara.com/instruments/gmr/

C.von Hebel, S. Rudolph, A. Mester, J.A. Huisman, P. Kumbhar, H. Vereecken, J. van der Kruk, Three-dimensional imaging of subsurface structural patterns using quantitative large-scale multiconfiguration electromagnetic induction data. Water Resour. Res. **50**, 2732–2748 (2014)

J.R. Wait, The magnetic diploe over the horizontally stratified earth. Can. J. Phys. **29**(6), 577–592 (1951)

D. Walsh, P. Turner, E. Grunewald, H. Zhang, J.J. Butler, E. Reboulet, S. Knobbe, T. Christy, J.W. Lane, C.D. Johnson, A small-diameter NMR logging tool for groundwater investigations. Groundwater **51**, 914–926 (2013)

M.M. Waxman, L.J.M. Smits, Electrical conductivity in oil-bearing shaly sand. Soc. Pet. Eng. J. **8**, 107–122 (1968)

J.-P. Wigneron, Y. Kerr, P. Waldteufel, K. Saleh, P. Richaume, P. Ferrazzoli, M.-J. Escorihuela, J.P. Grant, B. Hornbuckle, P. de Rosnay, J.-C. Calvet, T. Pellarin, R. Gurney, C. Mätzler, L-band microwave emission of the biosphere (L-MEB) model: Description and calibration against experimental data sets over crop fields. Remote Sens. Environ. **107**(4), 639 (2007)

X.Q. Yu, P.T. Wu, W.T. Han, Z.L. Zhang, A survey on wireless sensor network infrastructure for agriculture. Comput. Stand. Interfaces **35**(1), 59–64 (2013)

V. Zavorotny, S. Gleason, E. Cardellach, A. Camps, Tutorial on remote sensing using GNSS bistatic radar of opportunity. Geosci. Remote Sens. Mag. **2**(4), 8–45 (2014)

Q. Zhu, H. Lin, J. Doolittle, Repeated electromagnetic induction surveys for determining subsurface hydrologic dynamics in an agricultural landscape. Soil Sci. Soc. Am. J. **74**(5), 1750–1762 (2010)

M. Zreda, D. Desilets, T.P.A. Ferre, R.L. Scott, Measuring soil moisture content non-invasively at intermediate spatial scale using cosmic-ray neutrons. Geophys. Res. Lett. **35**(21), L21402 (2008)

M. Zreda, W.J. Shuttleworth, X. Zeng, C. Zweck, D. Desilets, T. Franz, R. Rosolem, COSMOS: The COsmic-ray soil moisture observing system. Hydrol. Earth Syst. Sci. **16**(11), 4079–4099 (2012)